A&A 570, A24 (2014)
DOI: 10.1051/0004-6361/201423632

Astronomy & Astrophysics

CO in Hickson compact group galaxies with enhanced warm H_2 emission: Evidence for galaxy evolution?⋆,⋆⋆

U. Lisenfeld[1,2], P. N. Appleton[3], M. E. Cluver[4,5], P. Guillard[6,7], K. Alatalo[3], and P. Ogle[8]

[1] Departamento de Física Teórica y del Cosmos, Universidad de Granada, Spain
e-mail: ute@ugr.es
[2] Instituto Universitario Carlos I de Física Teórica y Computacional, Facultad de Ciencias, 18071 Granada, Spain
[3] NASA Herschel Science Center, California Institute of Technology, Pasadena, CA 91125, USA
[4] Department of Astronomy, University of Cape Town, Private Bag X3, 7701 Rondebosch, South Africa
[5] ARC Super Science Fellow, Australian Astronomical Observatory, PO Box 915, North Ryde, NSW 1670, Australia
[6] Institut d'Astrophysique Spatiale, CNRS, UMR 8617, Université Paris-Sud, Bât. 121, 91405 Orsay Cedex, France
[7] Spitzer Science Center, IPAC, California Institute of Technology, Pasadena, CA 91125, USA
[8] NASA Extragalactic Database, IPAC, California Institute of Technology, Pasadena, CA 91125, USA

Received 13 February 2014 / Accepted 9 July 2014

ABSTRACT

Context. Galaxies in Hickson Compact Groups (HCGs) are believed to experience morphological transformations from blue, star-forming galaxies to red, early-type galaxies. Galaxies with a high ratio between the luminosities of the warm H_2 to the 7.7 μm PAH emission (so-called Molecular Hydrogen Emission Galaxies, MOHEGs) are predominantly in an intermediate phase, the green valley. Their enhanced H_2 emission suggests that the molecular gas is affected in the transition.
Aims. We study the properties of the molecular gas traced by CO in galaxies in HCGs with measured warm H_2 emission in order to look for evidence of the perturbations affecting the warm H_2 in the kinematics, morphology and mass of the molecular gas.
Methods. We observed the CO(1–0) emission of 20 galaxies in HCGs and complemented our sample with 11 CO(1–0) spectra from the literature. Most of the galaxies have measured warm H_2 emission, and 14 of them are classified as MOHEGs. We mapped some of these galaxies in order to search for extra-galactic CO emission. We analyzed the molecular gas mass derived from CO(1–0), M_{H_2}, and its kinematics, and then compared it to the mass of the warm molecular gas, the stellar mass and star formation rate (SFR).
Results. Our results are the following. (i) The mass ratio between the CO-derived and the warm H_2 molecular gas is in the same range as found for field galaxies. (ii) Some of the galaxies, mostly MOHEGs, have very broad CO linewidths of up to 1000 km s^{-1} in the central pointing. The line shapes are irregular and show various components. (iii) In the mapped objects we found asymmetric distributions of the cold molecular gas. (iv) The star formation efficiency ($=SFR/M_{H_2}$) of galaxies in HCGs is very similar to isolated galaxies. No significant difference between MOHEGs and non-MOHEGs or between early-type and spiral galaxies has been found. In a few objects the SFE is significantly lower, indicating the presence of molecular gas that is not actively forming stars. (v) The molecular gas masses, M_{H_2}, and ratios M_{H_2}/L_K are lower in MOHEGs (predominantly early-types) than in non-MOHEGs (predominantly spirals). This trend remains when comparing MOHEGs and non-MOHEGs of the same morphological type.
Conclusions. We found differences in the molecular gas properties of MOHEGs that support the view that they have suffered (or are presently suffering) perturbations of the molecular gas, as well as a decrease in the molecular gas content and associated SFR. Higher resolution observations of the molecular gas are needed to shed light on the nature of these perturbations and their cause.

Key words. galaxies: evolution – galaxies: groups: general – galaxies: ISM – galaxies: interactions – infrared: galaxies – intergalactic medium

1. Introduction

Compact groups represent the highest density enhancements outside clusters. Galaxies within them have relatively low velocity dispersions (median dispersion ~200 km s^{-1}, Hickson et al. 1992) which makes compact groups ideal objects to study the influence of the environment and interaction on galaxy properties and morphological evolution. Hickson (1982) selected a uniform sample of 100 nearby compact groups (Hickson compact groups, hereafter HCGs) consisting of four to eight members which have been extensively studied since then.

HCGs show a high ratio of early-type to spiral galaxies (the spiral fraction is about 50% compared to that of field galaxies, Hickson 1982) which suggests that morphological transformations from late-type to early-type galaxies are taking places. It has been proposed (e.g. Quilis et al. 2000; Bekki & Couch 2011), that S0 galaxies in HCGs might be stripped spirals. It is, however, still completely unclear what the dominant mechanism for such a morphological evolution could be. Different scenarios for the transformation of spirals into S0s in groups and clusters have been proposed, which include ram pressure stripping (e.g. Gunn & Gott 1972; Farouki & Shapiro 1980; Abadi et al. 1999), tidal encounters (e.g. Icke 1985; Bekki & Couch 2011), truncation of gas replenishment (e.g. Larson et al. 1980; Bekki et al. 2002), minor and unequal-mass merging (e.g. Bekki 1998)

⋆ Table 5 and Appendix A are only available in electronic form at http://www.aanda.org
⋆⋆ Spectra from Figs. A.1 and A.2 and the FITS files of the reduced spectra are only available at the CDS via anonymous ftp to cdsarc.u-strasbg.fr (130.79.128.5) or via http://cdsarc.u-strasbg.fr/viz-bin/qcat?J/A+A/570/A24

and harassment combined with interaction with intergalactic gas (Cluver et al. 2013).

Observations of the atomic hydrogen (HI) have provided further evidence for strong interactions. Many HCGs show a considerable amount of intergalactic HI and at the same time an HI deficiency, both globally for the groups as well as individually for their members (Verdes-Montenegro et al. 2001). The fate of this missing gas is still unclear, even though deep single-dish observations discovered a low surface brightness HI component, missed by interferometric observations, which can reduce, but not completely eliminate, the HI deficiency (Borthakur et al. 2010). Recent *Herschel* observations (Bitsakis et al. 2014) of 28 HCGs give further support for the presence of intergalactic material, discovering intergalactic dust in 4 groups and finding that a fraction of 15–20% of the 250 μm emission resides outside of the main body of late-type and lenticular galaxies. Observations of the CO emission of galaxies in HCGs showed a much less dramatic picture. Leon et al. (1998) found a slight enhancement of M_{H_2}/L_B of galaxies in HCGs compared to a sample of field and interacting galaxies. On the contrary, Verdes-Montenegro et al. (1998) found no evidence for an enhancement of M_{H_2} in HCGs compared to a sample of isolated galaxies, whereas Verdes-Montenegro et al. (2007) found tentative evidence of a depressed molecular gas content in HI deficient galaxies in HCGs. Martinez-Badenes et al. (2012) solved these apparent contradictions by showing that there is an enhancement of ~0.2 dex in M_{H_2}/L_K compared to isolated galaxies. They found tentative evidence that this enhancement was mainly in groups in an early evolutionary phase, whereas in galaxies in more evolved groups the molecular gas mass was the same as in isolated galaxies. They speculated on an evolutionary sequence in which the molecular gas mass was enhanced in early stages due to tidal interaction and later M_{H_2} decreased either due to gas depletion or environmental effects.

Further evidence for evolution in HCGs came from Johnson et al. (2007) who found an infrared "gap", i.e. a seemingly underpopulated region, in the *Spitzer* Space Observatory IRAC color diagram in the region separating actively starforming, blue galaxies from red galaxies dominated by an evolved stellar population. This gap is not found in comparison samples (e.g. the *Spitzer* Infrared Nearby Galaxies Survey (SINGS) sample). The low density of galaxies in this "gap" suggests that the evolutionary phase corresponding to the gap is a very short transition. The existence of an underpopulated region was confirmed in larger samples (Walker et al. 2010, 2012) but reduced in extension to a smaller area in the mid-IR colors (Walker et al. 2012).

Cluver et al. (2013) studied a sample of Hickson Compact Groups (HCGs) with intermediate HI deficiencies and identified a number of galaxies with enhanced warm H_2 emission, well above the level expected from star formation (SF) and indicative of shock-excitation, classifying them as co-called Molecular Hydrogen Emission Galaxies (MOHEGs; Ogle et al. 2010). Interestingly, most of these galaxies have IRAC colors in the range of the previously found gap (Johnson et al. 2007; Walker et al. 2010). Furthermore, based on their extinction-corrected optical colors, these galaxies fall predominantly in the "green valley" between blue, starforming galaxies and red-sequence objects. Cluver et al. (2013) conclude that the increased warm H_2 emission is most likely due to shock-excitation. They propose that these galaxies might be in a special phase of their evolution in which interaction with material from the IGM – most likely previously stripped gas – causes viscous stripping and shock-excitation of the molecular gas. This event could be important for their further evolution and might even trigger their evolution from the blue cloud to the red sequence.

Enhanced H_2 emission had previously been found in one of the most spectacular HCGs, Stephan's Quintet (HCG 92; Appleton et al. 2006; Cluver et al. 2010) where it originated in an intergalactic region dominated by gas interaction producing large scale shocks. Guillard et al. (2009) showed that H_2 can form in the dense, post-shock gas and that its luminosity can be powered by the dissipation of turbulent energy after the energy injected on large scales by the galaxy collision cascades on smaller scales. Not only warm H_2 gas, emitting in the mid-infrared, but also molecular gas traced by the CO(1–0) line was found abundantly in this region, with velocities showing that it is present both in the pre- and in the post-shock gas (Guillard et al. 2012). This component of the molecular gas carries a significant fraction of the total kinetic energy.

All these results suggest that the molecular gas plays an important role in processes that are relevant to galaxy evolution. The warm molecular gas seems to be a tracer for galaxies in a transitionary phase. The observations of Stephan's Quintet show that the warm and the cold (CO traced) molecular gas[1] are closely related. So far no study has focussed on the molecular gas content in galaxies in HCGs that have been selected based on their warm H_2 emission. In order to address this issue, in the present paper, we present and analyze CO observations for a sample of galaxies in HCGs with existing warm H_2 data. We chose a subsample of the galaxies studied by Cluver et al. (2013) which includes both galaxies with an enhanced warm H_2 emission (MOHEGs) and galaxies in which the H_2 emission can be explained by SF. The goal of our work is to characterize the properties of the CO-traced ("cold") molecular gas in a sample with information on the luminosity and mass of the warm molecular gas in order to study the relation between both emissions and look for evidence of differences between MOHEGs and non-MOHEGs that could help to better understand the mechanisms responsible for galaxy evolution in HCGs.

2. The sample

We selected our sample from the galaxies studied by Cluver et al. (2013) who carried out a *Spitzer* mid-infrared spectroscopic study of 74 galaxies located in 23 HCGs. Their sample selected groups with intermediate HI deficiencies because those are expected to be most likely in an active phase of transformation. Table 1 lists the groups included in our study together with some general group properties. Furthermore, only groups with visible signs of tidal interaction in two or more group members were included in their sample. Their study allowed to measure the ratio of the warm H_2 luminosity (summed over the 0–0S(0) to 0–0S(3) lines) to the 7.7 μm PAH luminosity, hereafter referred to as H_2/7.7 μm.

We observed 20 of these galaxies with the IRAM 30 m telescope, selecting preferentially those galaxies with a high H_2/7.7 μm ratio. This ratio can be used as an indicator of whether the warm H_2 emission is due to UV excitation

[1] Throughout this paper we call the molecular gas derived from the CO(1–0) emission the "cold" molecular gas, in contrast to the warm molecular gas derived from the H_2 emission, and we denote it as M_{H_2} $M_{H_2,0}$, or $M_{H_2,tot}$, whereas we call the warm molecular gas explicitly $M_{H_2,warm}$. We note, however, that CO(1–0) can trace relatively warm H_2 gas and that, without additional measurements, we cannot determine the physical temperture of the CO(1–0) emitting gas. Therefore, the above naming has to be understood as a pure convention without meaning real physical tempertures.

Table 1. Basic data of the groups.

Group	z^a	Θ^b [arcmin]	$\log(\sigma_v)^c$ [km s^{-1}]	$\log(R)^d$ [kpc]	$\log(L_B)^e$ [W]	$\log(M_{HI})^f$ [$M_\odot$]	HI deficiency^f	$\log(M_{star})^g$ [$M_\odot$]	$\log(M_{dyn})^h$ [$M_\odot$]
HCG 6	0.0379	1.60	2.40	1.54	37.58	9.71	0.33	11.30	12.63
HCG 15	0.0228	7.70	2.63	2.03	37.63	9.59	0.46	11.04	13.19
HCG 25	0.0212	6.40	1.79	1.82	37.38	>10.15	<0.02	10.96	11.11
HCG 31	0.0135	0.90	1.75	1.04	37.38	10.36	0.18	–	–
HCG 40	0.0223	1.70	2.17	1.32	37.66	9.84	0.29	11.56	12.27
HCG 44	0.0046	16.40	2.13	1.72	37.12	8.98	0.76	10.75	12.68
HCG 47	0.0317	2.30	1.63	1.70	37.44	9.95	0.28	11.24	11.60
HCG 55	0.0526	0.90	2.33	1.42	37.71	–	–	11.39	12.49
HCG 56	0.0270	2.10	2.23	1.47	37.47	9.38	0.73	10.92	12.78
HCG 57	0.0304	5.50	2.43	2.00	37.98	9.73	0.86	11.70	12.55
HCG 67	0.0245	3.30	2.32	1.83	37.92	9.69	0.62	11.43	12.13
HCG 68	0.0080	9.20	2.19	1.66	37.54	>9.77	<0.12	11.29	12.80
HCG 79	0.0145	1.30	2.14	0.97	37.17	9.64	0.08	10.80	11.68
HCG 82	0.0362	3.10	2.79	1.99	37.89	<9.71	>0.76	11.54	13.01
HCG 91	0.0238	5.20	2.26	1.86	37.89	10.38	0.20	11.13	12.64
HCG 95	0.0396	1.50	2.49	1.62	37.80	>10.12	<0.21	11.22	12.67
HCG 96	0.0292	2.30	2.12	1.62	37.76	>10.22	<0.17	–	–
HCG 100	0.0178	3.60	1.95	1.72	37.24	>9.97	<0.28	10.79	11.13

Notes. [a] Redshift from NED. [b] Angular size (Hickson 1982). [c] Radial velocity dispersion (Hickson et al. 1992). [d] Median projected distance from Hickson et al. (1992), adapted to our distance. [e] Blue luminosity, from Hickson et al. (1992), adapted to our distance. [f] Total HI mass, adapted to our distance, and HI deficiency defined as $\log(M(\mathrm{HI})_{\mathrm{predicted}}$–$\log(M(\mathrm{HI})_{\mathrm{observed}}$, from Borthakur et al. (2010), if available, or otherwise from Verdes-Montenegro et al. (2001). [g] Total stellar mass, from Bitsakis et al. (2011), adapted to our distance. [h] Dynamical mass, from Bitsakis et al. (2011), adapted to our distance.

(H_2/7.7 μm $\sim$ 0.01 or below) or due to dissipation of turbulent kinetic energy (H_2/7.7 μm $\gtrsim$ 0.01) (Guillard et al. 2012). We adopt the definition of Ogle et al. (2010) that a molecular hydrogen emission galaxy (MOHEG) has H_2/7.7 μm $>$ 0.04, which is also used in Cluver et al. (2013). For 11 additional galaxies CO data from the literature is available, mostly from the IRAM 30 m telescope. Thus, our complete sample includes 31 galaxies in 18 groups and spans a large range of HI depletion ranging from $0 \leq \log(M(\mathrm{HI})_{\mathrm{pred}}) - \log(M(\mathrm{HI})_{\mathrm{obs}}) \leq 0.97$. In Table 2 we list the galaxies in the sample together with some general properties.

3. The data

3.1. CO observations and reduction

We observed the CO(1–0) and CO(2–1) lines at 115 and 230 GHz between June and September 2011 with the IRAM 30 m telescope on Pico Veleta. We used the EMIR dual-polarization receivers, with the autocorrelator WILMA as backend. This setup yields a resolution of 2 MHz and a bandwidth of 3.7 GHz. All observations were performed in wobbler-switching mode, with a throw in azimuth between 150 and 240″, chosen carefully to avoid any other galaxies in the group at the off-position. The telescope pointing was checked on a nearby quasar about every 90 min. The average pointing offset was 3–4″.

All observations were carried out in good weather conditions, the mean system temperatures being 200 K for the CO(1–0) and 290 K for the CO(2–1) transition on the T_A^* scale. All CO spectra and intensities are presented on the main beam temperature scale (T_{mb}) which is defined as $T_{mb} = (F_{eff}/B_{eff}) \times T_A^*$. The main beam efficiencies are 0.77 (115 GHz), and 0.58 (230 GHz), with half-power beam widths of about 22″ (115 GHz), and 11″ (230 GHz).

Most of the galaxies were only observed at their central position, but some were mapped (HCG 25b, HCG 40c, HCG 91a and HCG 57a). We selected a galaxy for mapping if its central CO emission was bright and its size was considerably larger than the IRAM CO(1–0) beam. A further criterion was the presence of strong warm H_2 emission either in the centre or at an off-centre position. In Figs. 3–6 the observed positions are overlaid over IRAC three-color images of the galaxies. In two of these objects, one of the mapped positions coincides very accurately with the central position of a neighbouring galaxy. This is the case for the position (–3, –33) in HGC 25b which coincides exactly with the central position in HCG 25f and the position (15, 15) in HCG 57a which is 1″ away from the central position in HGC 57d. In the following we identify these positions with the corresponding neighbouring galaxies HCG 25f and HCG 57a. In the case of HCG 31ac, the CO spectrum taken from the literature (Leon et al. 1998) corresponds to the position of HCG 31c. At the position of HCG 31a only an upper limit was observed (Martinez-Badenes et al. 2012). Since the objects HCG 31a and HCG 31c are in the process of merging and very close to each other (distance of the centres 16″), we follow the convention suggested in Gallagher et al. (2010) to consider both objects as a merger blend and call it HCG 31ac.

The data were reduced in the standard way using the CLASS software in the GILDAS package[2]. We selected the observations with a good quality (taken during satisfactory weather conditions and showing a flat baseline), averaged the spectra over the individual positions and subtracted a baseline which was a constant continuum level for the CO(1–0) spectra and a linear baseline for the CO(2–1) data.

In order to check the relative calibration, we observed the central position of HCG 68c, HCG 91a and HCG 96a, which exhibit strong CO(1–0) and CO(2–1) lines, on different days. The agreement between the velocity integrated line intensities of CO(1–0), $I_{CO(1-0)}$, is better than 10% most of the time, with the exception of one day where the disagreement is 30%. The

[2] http://www.iram.fr/IRAMFR/GILDAS

Table 2. Basic data of the sample galaxies.

Galaxy	D^a [Mpc]	T(RC3)^b	$D_{25}{}^c$ [′]	i^d [°]	$\log(L_K)^e$ $L_{\odot,k}$
HCG 6b	155.65	1	0.87	51	11.09
HCG 6c	155.65	–3	0.91	90	–
HCG 15a	93.64	–2	1.29	74	11.17
HCG 15d	93.64	–3	0.91	44	10.72
HCG 25b	87.07	1	0.95	56	11.06
HCG 25f	87.07	–2	0.43	56	10.11
HCG31ac	55.44	9	1.00	80	10.08
HCG 40b	91.58	–3	0.89	53	10.93
HCG 40c	91.58	2	1.55	90	11.09
HCG 40d	91.58	0	0.91	81	10.92
HCG 44a	18.89	1	3.63	87	10.84
HCG 44d	18.89	5	2.24	74	9.35
HCG 47a	130.19	2	1.02	66	11.19
HCG 47d	130.19	7	0.50	32	10.51
HCG 55c	216.02	1	0.62	54	11.24
HCG 56b	110.88	0	0.76	62	11.07
HCG 56c	110.88	–2	0.81	48	10.78
HCG 57a	124.85	2	1.62	90	11.54
HCG 57d	124.85	3	0.55	36	10.85
HCG 67b	100.62	3	1.07	88	11.03
HCG 68a	32.85	–2	2.40	80	10.98
HCG 68b	32.85	–2	3.02	90	–
HCG 68c	32.85	4	2.69	54	10.92
HCG 79a	59.55	0	1.78	16	10.57
HCG 79b	59.55	–2	2.29	67	10.55
HCG 82b	148.67	–2	0.89	55	11.27
HCG 82c	148.67	8	0.72	90	10.97
HCG 91a	97.74	5	1.95	47	11.58
HCG 95c	162.63	9	0.74	78	10.92
HCG 96a	119.92	4	1.12	0	–
HCG100a	73.10	0	0.87	60	11.13

Notes. $^{(a)}$ Distance, based on redshifts from the NASA/IPAC Extragalactic Database (NED) listed in Cluver et al. (2013) and adopting a Hubble constant of 73 km s^{-1} Mpc^{-1}. $^{(b)}$ Morphological type taken from the LEDA database, following the RC3 classification (de Vaucouleurs et al. 1991). $^{(c)}$ Optical major diameter at the 25 mag arcsec^{-2} isophot taken from LEDA. $^{(d)}$ Inclination taken from LEDA. $^{(e)}$ Decimal logarithm of the luminosity in the K-band in units of the solar luminosity in the K_S-band ($L_{K,\odot} = 5.0735 \times 10^{32}$ erg s^{-1}). We calculated the K_S luminosity, L_K, from the total (extrapolated) K_S flux, f_K, as $L_K = \nu f_K(\nu)$ (where ν is the frequency of the K-band, 1.38×10^{14} Hz). The fluxes in the K_S (2.17 μm) band were taken from Bitsakis et al. (2011) who obtained them partly from their own observations and partly from the 2MASS Extended Source Catalog (Jarrett et al. 2000).

Table 3. *Spitzer* data.

Galaxy	$f_{5.8}/f_{3.6}{}^a$	$H_2/7.7\,\mu m^b$	$f_{24\ \mu m,tot}{}^c$ [mJy]	$f_{24\ \mu m,CObeam}{}^d$ [mJy]
HCG 6b	–0.25	0.198	3.80 ± 0.19	2.53 ± 0.08
HCG 6c	–0.38	–	0.80 ± 0.04	1.32 ± 0.08
HCG 15a	–0.29	0.044	5.60 ± 0.28	4.20 ± 0.09
HCG 15d	–0.30	0.112	2.70 ± 0.14	3.72 ± 0.10
HCG 25b	–0.24	0.098	4.70 ± 0.24	5.69 ± 0.07
HCG 25f	–0.36	–	–	0.70 ± 0.07
HCG31ac	0.32	0.002	–	307.68 ± 0.14
HCG 40b	–0.34	0.083	3.00 ± 0.15	9.07 ± 0.07
HCG 40c	0.09	0.010	73.40 ± 3.67	35.08 ± 0.07
HCG 40d	0.06	0.013	88.10 ± 4.41	67.71 ± 0.07
HCG 44a	–0.20	0.042$^{(1)}$	246.00 ± 12.30	73.85 ± 0.06
HCG 44d	0.19	0.021	79.90 ± 4.00	19.80 ± 0.06
HCG 47a	–0.01	0.035	87.00 ± 4.35	38.00 ± 0.13
HCG 47d	–0.19	–	4.50 ± 0.23	4.70 ± 0.13
HCG 55c	–0.01	0.018	7.70 ± 0.39	6.13 ± 0.07
HCG 56b	0.16	0.053	185.00 ± 9.25	134.56 ± 0.07
HCG 56c	–0.32	0.037	0.90 ± 0.05	10.39 ± 0.07
HCG 57a	–0.27	0.174	13.80 ± 0.69	9.63 ± 0.05
HCG 57d	0.03	–	24.00 ± 1.20	15.50 ± 0.05
HCG 67b	0.02	0.006	84.80 ± 4.24	32.65 ± 0.07
HCG 68a	–0.35	0.741	21.30 ± 1.07	14.63 ± 0.05
HCG 68b	–0.35	0.073	9.80 ± 0.49	7.79 ± 0.05
HCG 68c	0.01	0.044	403.60 ± 20.18	122.81 ± 0.06
HCG 79a	–0.06	0.011	23.30 ± 1.17	17.25 ± 0.05
HCG 79b	–0.18	0.010	33.70 ± 1.69	27.95 ± 0.05
HCG 82b	–0.31	0.045	5.80 ± 0.29	3.76 ± 0.04
HCG 82c	0.41	0.014	90.60 ± 4.53	63.30 ± 0.04
HCG 91a	0.09	0.030	351.00 ± 17.55	184.46 ± 0.06
HCG 95a	–0.08	0.071	19.80 ± 0.99	15.17 ± 0.07
HCG 96c	0.37	0.007	–	473.06 ± 1.40
HCG100a	–0.05	0.013	153.00 ± 7.65	102.47 ± 0.08

Notes. $^{(1)}$ Value taken from Roussel et al. (2007). $^{(a)}$ IRAC flux ratio. $^{(b)}$ Ratio between luminosity of the total (sum of S(0)–S(3) lines) warm H_2 emission and the 7.7 μm PAH feature. If $H_2/7.7\,\mu m > 0.04$ the galaxy is classified as a MOHEG (Ogle et al. 2010). $^{(c)}$ Total 24 μm flux of the galaxy and its error, taken from Bitsakis et al. (2011). $^{(d)}$ 24 μm flux within the IRAM CO(1–0) beam (see text) and its photometric error, derived from the rms of the background. In addition, a calibration error of 10% error (Engelbracht et al. 2007) has to be taken into account.

reason for this poorer calibration agreement is not entirely clear, possibly it was caused by a slight pointing offset in one of the observations. The agreement for the CO(2–1) line intensities, $I_{CO(2-1)}$, is between 15 and 30%. Based on these measurements we adopt a (probably conservative) calibration error of 20% for $I_{CO(1-0)}$ and 30% for $I_{CO(2-1)}$.

3.2. Spitzer data

Our analysis made use of *Spitzer* Space Observatory IRAC and MIPS data. We took the total IRAC fluxes of the galaxies from Cluver et al. (2013; their Table 4), which were obtained with aperture photometry covering the entire galaxies, and applied the k-correction derived by these authors. We furthermore took the ratio between H_2 luminosity and the luminosity in the 7.7 μm band, $H_2/7.7\,\mu$m, from these authors (their Table 2).

We took the total MIPS 24 μm fluxes from Bitsakis et al. (2011, their Table 1). A few objects are missing in their sample (HCG 31ac and HCG 96a) or no 24 μm data is given (HCG 25f). We did not attempt to derive the total fluxes for these objects because either the emission is very weak so that no reliable total flux can be derived, or the galaxies are so close to a neighboring object that no separate total emission can be derived.

In addition, we derived the 24 μm flux within the IRAM CO(1–0) beam directly from the MIPS images in order to locally compare this SF tracer to the molecular gas mass. To achieve this, we multiplied the MIPS 24 μm image with the IRAM beam pattern (approximated as a normalized Gaussian beam) placed at the position where the CO beam was pointed, and measured the total 24 μm emission of this map. We used a FWHM of 21″ in order to achieve, after convolution with the 24 μm map (spatial resolution 5.9″), a total FWHM of 22″which corresponds to the FWHM of the IRAM beam at the frequency of our observations.

Some of our objects habor AGNs (HCG 47a, 56B, 57a, 91A, 95C and 96A, from Table 3 in Cluver et al. 2013) and their 24 μm flux might be affected by this. In order to avoid a contribution of the AGN to the 24 μm emission which would produce

Table 4. Warm molecular gas mass.

Galaxy	Lines[a]	T_1[b] [K]	OPR_1[c]	$\log(M_1)$[d] [$M_\odot$]	T_2[b] [K]	OPR_2[c]	$\log(M_2)$[d] [$M_\odot$]	$\log(M_{1+2})$ [$M_\odot$]	H_2 Dimensions[e] [$''^2$]	f_{corr}[f]	$\log(M_{H_2,warm})$[g] [$M_\odot$]
HGC 6b	0123(45)	163	2.6	7.91	792	3	5.3	7.91	15.3 × 5.4	1.00	7.91
HGC 15a	(0)135	139	2.4	7.69	1044	3	4.46	<7.69	30.6 × 14.4	1.01	<7.70
HGC 15d	0123(4)5	150	2.5	7.78	630	3	5.30	7.78	25.5 × 7.2	0.86	7.72
HGC 25b	(0)1	173	2.7	7.39	–	–	–	<7.39	20.4 × [10.2]	1.00	<7.39
HGC 31ac	(0)1	268	3.0	5.02	–	–	–	<5.02	10.2 × [10.2]	1.00	<5.02
HGC 40b	(0)1(2)34(5)	142	2.4	7.71	911	3	4.11	<7.71	20.4 × 3.6	1.00	<7.71
HGC 40c	01	157	2.6	8.60	–	–	–	8.60	40.8 × [10.2]	0.54	8.33
HGC 40d	0123(4)5	144	2.4	8.26	482	3	6.18	8.26	20.4 × 9.0	1.00	8.26
HGC 44a	01	158	2.6	7.53	–	–	–	7.53	61.2 × [10.2]	0.36	7.08
HGC 44d	01(234)5	141	2.4	7.18	577	3	5.40	7.18	51.0 × [10.2]	0.43	6.81
HGC 47a	(0)12(3)4(5)	145	2.4	8.60	935	3	5.85	<8.60	35.7 × [10.2]	0.62	<8.39
HGC 47d	(0)12(3)4(5)	100	1.6	8.81	799	3	6.40	<8.81	22 × 22	1.00	<8.81
HGC 55c	01234(5)	158	2.6	7.99	1031	3	5.30	7.99	10.2 × 7.2	1.00	7.99
HGC 56b	(0)12(34)5	–	–	–	540	3	3.22	<6.32	35.7 × [10.2]	0.62	<6.11
HGC 56c	(0)1(2)3(4)5	154	2.5	7.54	779	3	5.15	<7.54	15.3 × 10.8	1.00	<7.54
HGC 56e	(0)1(2)3(4)5	113	1.9	8.44	1365	3	3.96	<8.44	22 × 22	1.00	<8.44
HGC 57a	01	206	2.9	8.25	–	–	–	8.25	40.8 × [10.2]	0.54	7.98
HGC 67b	01234(5)	141	2.4	6.81	1169	3	3.58	6.81	25.5 × [10.2]	0.86	6.75
HGC 68a	(0)123(45)	100	1.6	7.18	429	3	5.51	<7.19	25.5 × 10.8	0.86	<7.12
HGC 68b	(0)1(2)3(45)	140	2.4	6.81	1169	3	3.60	<6.81	20.4 × 10.8	1.00	<6.81
HGC 68c	0123(45)	100	1.6	7.89	415	3	6.00	7.90	71.4 × 68.4	0.52	7.62
HGC 79a	0123(4)(5)	123	2.1	7.77	400	3	5.83	7.77	20.4 × 10.8	1.00	7.77
HGC 79b	0123(4)5	193	2.8	6.70	–	–	–	6.70	15.3 × 7.2	1.00	6.70
HGC 82b	01(2)3(45)	115	1.9	8.28	373	3	6.28	8.29	15.3 × 3.6	1.00	8.29
HGC 82c	0123(4)5	156	2.6	8.64	652	3	6.04	8.64	10.8 × 12.6	1.24	8.74
HGC 91a	0123(4)5	151	2.5	8.48	1058	3	5.18	8.48	45.9 × [10.2]	0.48	8.16
HGC 95c	0123(4)5	140	2.4	8.18	605	3	6.15	8.19	20.4 × 19.8	1.94	8.48
HGC 96a	0123(4)5	100	1.6	9.58	–	–	–	–	9.58 × 45.9	0.48	9.26
HGC 100a	01234(5)	194	2.8	7.47	1057	3	4.83	7.47	35.7 × 10.8	0.62	7.26

Notes. No measurements for HCG 6c, HCG 25f and HCG 57d are available. [(a)] Number of the observed lines, n denotes the transition 0–0S(n). A parenthesis indicates that the line was not detected so that only an upper limit could be measured. [(b)] Temperture of coolest component (T_1), and the second, hotter (T_2) component derived from the fit to the excitation diagrams. [(c)] Ortho-to-para ratio determined from the fit. [(d)] Logarithm of the mass of each component determined over the extracted area. This mass is an upper limit if the lowest line, 0–0S(0), is not detected. [(e)] Dimension of the warm H_2 emission, measured where possible in orthogonal LL and SL IRS slits. If no SL slit measurement was available, the width of the LL slit was assumed and the width is given in parenthesis. [(f)] Correction factor, which corrects IRS observations for the geometry of the extraction area relative to the LL slit width and to the IRAM beam (see text for a more detailed explanation). [(g)] Logarithm of the mass of the warm molecular gas within the IRAM 30 m CO(1–0) beam. If the S(0) line is an upper limit, the mass is an upper limit (see text).

an overestimate of the SFR (see Sect. 4.6) we inspected the 24 μm images of these galaxies and searched for strong, centrally concentrated emission indicative of an AGN. HCG 56b and HCG 96a show intense, point-like 24 μm emission in the centre. The central emission in HCG 56b is so bright that the value of $f_{24\ \mu m,CObeam}$ for the neighboring galaxy, HCG 56c, is strongly affected. We therefore excluded all three objects from the analysis of the SFR and star formation efficiency (SFE). In the other objects no indication of a contribution of the AGN to the 24 μm was noticeable.

The fluxes are listed in Table 3. For some objects the flux within the CO beam is larger than the total flux. This is because our value for $f_{24\ \mu m,CObeam}$ can include the emission of nearby objects if they are strong and close-by, whereas Bitsakis et al. (2011) have attempted to separate the flux for the two.

3.3. Properties of the warm molecular gas from Spitzer observations.

The properties of the warm molecular gas were derived from the strength and extent of the detected pure-rotational 0–0S(0) to 0–0S(5) lines of molecular hydrogen from the observations of Cluver et al. (2013) where the full details of the observations are given. Table 4 lists the derived properties of the warm H_2 gas for each galaxy. In order to measure the masses and temperature of the warm molecular hydrogen we constructed excitation diagrams (see for example Rigopoulou et al. 2002). The excitation diagrams plot the column density of H_2, N, in the upper level of each transition, normalized by its statistical weight, g, versus the upper level energy for each rotational H_2 line observed by *Spitzer*. The diagrams can be used to estimate the total column density and temperature of the warm H_2 within the slit for each galaxy observed. Gas with a constant temperature would appear as a linear distribution of points in the excitation diagram after correcting for an assumed ortho-to-para ratio.

Figure 1A shows an example (from HCG 57a) where we have detected all 6 rotational lines and have the best constraints on the H_2 temperatures and column densities. A problem stems from the sparse sampling of the excitation diagram in some slit positions. Figure 1B (HCG 15a) shows an examples where we did not detect some of the transitions and only have upper limits. In this case, if only the detected points are used, the slope of the fit is shallow leading to a higher temperature for the gas, and a low mass. However, if we assume the 0–0S(0) line (at 28 μm) is detected we can perform a two-temperature fit and determine an effective upper limit for the H_2 mass, since pushing

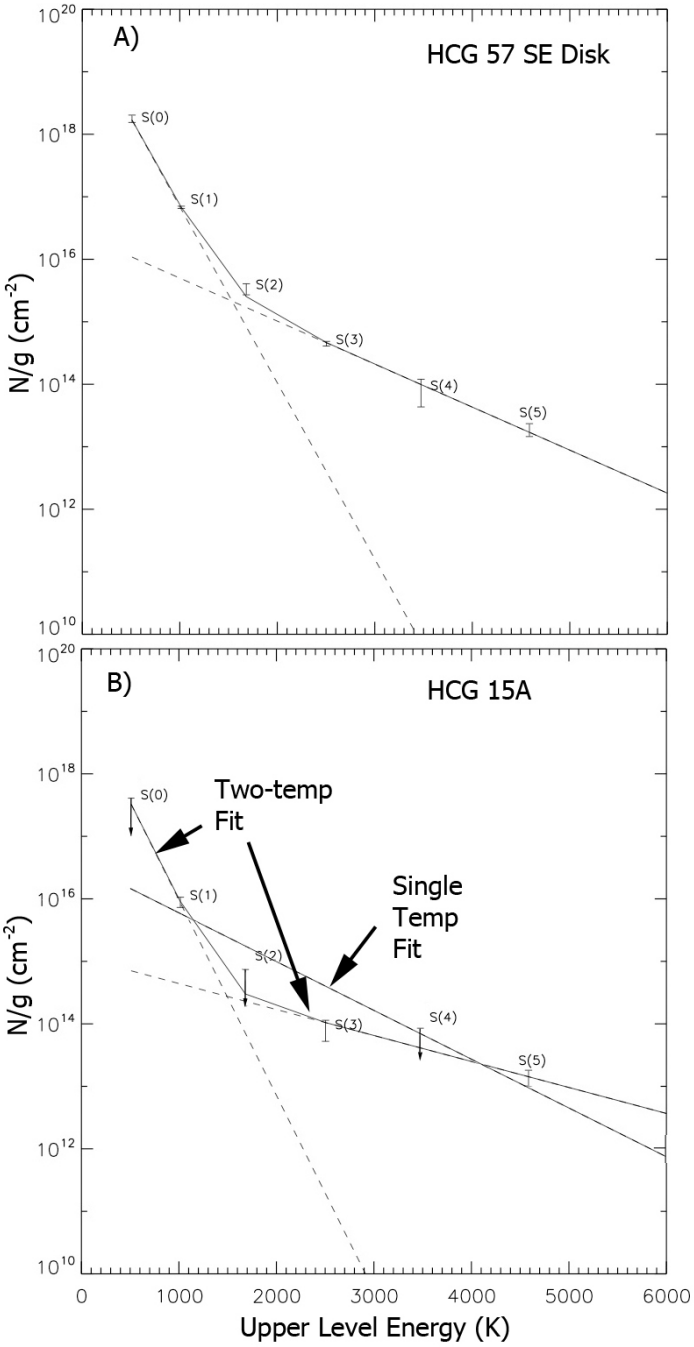

Fig. 1. Examples of the temperature fit to the excitation diagram showing the column density of the upper level of each transition normalized by its statistical weight versus the upper level energy (see text for further discussion of these figure.) *Top*: case where H_2 is detected at all levels S(0)–S(5). *Bottom*: case where several upper limits are present.

the detection down to lower values would increase the temperature of the low-temperature component, decreasing its mass. In Table 4, we have indicated cases where we have used the upper limit to the detection of 0–0S(0) as an upper-limit to the mass using this technique.

We have assumed a thermal equilibrium value (LTE) for the ortho-to-para ratio of the H_2. For temperatures above 300 K this ratio is 3, but varies to lower values of ortho-to-para ratio in LTE for lower temperatures (see Wilgenbus et al. 2000). Thus we interactively fit the excitation diagram points, allowing for lower values of ortho-to-para ratio as we home-in on a solution. In some cases we do not have enough points on the excitation diagram to detect an offset between the ortho- and para-transitions that would result from non-LTE conditions. In those cases we assume LTE conditions, and accept an unknown uncertainty in the derived H_2 masses. This may be justified, since in those cases where we have enough points to notice an offset between the odd and even transitions, we do not see any systematic deviations from LTE.

Warm H_2 masses were estimated for each galaxy by multiplying the derived column densities with the linear extent of the emission. Most objects were covered by a combination of perpendicular slits, an 10.2″ wide Long-Low (LL) slit and a 3.6″ wide Short-Low (SL) slit. We assumed for the extent of the H_2 emission the linear extent in the LL slit times its slit width of 10.2″. In those cases where also SL measurements were available, we could directly measure the perpendicular extension and applied a correction factor f_1 = SL extension (in arcsec)/10.2″ if the extension in the SL slit was found to be different from the 10.2″ width of the perpendicular LL slit. In order to compare our warm H_2 results to the cold H_2 masses derived from the IRAM telescope, we applied a second correction factor, a beam correction factor, f_2. This factor depends on the assumed distribution of warm H_2, varying from the case where all the warm H_2 lies within the 22″ × 22″ IRAM beam (no correction), to cases where the H_2 is extended in one or (rarely) both dimensions relative to the IRAM beam. Approximate H_2 dimensions were obtained from the extent of the H_2 in both the LL and SL slits (tabulated by Cluver et al. 2013). The total correction factor was then $f_{\rm corr} = f_1 \times f_2$. It varies from unity in most cases, to the largest correction of 0.36 for HCG 44a, where the H_2 emission is highly elongated along the direction of the LL slit compared with the 22″ IRAM beam.

The assumption and limitations in the data produce, in some cases, a considerable uncertainty in the derived warm molecular gas mass. This uncertainty is difficult to quantify precisely, especially in the cases where a correction factor was applied, but we can estimate it. The error of the H_2 line fluxes is about 10%, and the error in the mass determination for those cases where no correction factor was applied about 20%. We estimate the error introduced by the correction factor to be ∼30% on average so that in these cases the total error of the warm H_2 mass is about 40%.

4. Results

4.1. CO spectra, integrated intensities and kinematics

In Appendix A we show the spectra of the detections and tentative detection of CO(1–0) and CO(2–1). For each spectrum, we integrated the intensity along the velocity interval where emission is detected. For nondetections we set an upper limit as

$$I_{\rm CO} < 3 \times {\rm rms} \times \sqrt{\delta V\, \Delta V}, \quad (1)$$

where δV is the channel width, ΔV the total line width and rms the root mean square noise. When the source is detected in only one transition, this line width is used to calculate the upper limit in the other transition. In case of nondetection of both lines, the mean value of all detections was used as an estimate for the linewidth (ΔV = 470 km s^{-1} for CO(1–0) and ΔV = 410 km s^{-1} for CO(2–1)). The results of our CO(1–0) and CO(2–1) observations are listed in Table 5.

The zero-level line widths of the detected spectra range from ∼150 to 950 km s^{-1}. Most noticeable are two MOHEGs,

HCG 68a and HCG 57a, with very broad (>800 km s^{-1}) lines. Also HCG 55c, a galaxy with enhanced H_2 emission, slightly below the MOHEG threshold, has a broad spectrum of 730 km s^{-1}. Their spectra have an irregular profile with indications of different components. A possible reason for the broad lines could be a projection effect, i.e. the presence of an additional molecular gas component not associated with galaxy rotation, e.g. infalling or outflowing molecular gas or gas displaced by tidal effects. Higher resolution CO observations are necessary to resolve this issue. In the case of HCG 57a, interferometric observations with CARMA have been carried out (Alatalo et al. 2014) and shown that the position-velocity diagram is not well described by rotation alone, but has an additional component which seems to trace outflowing or infalling gas.

The average value for the line ratio is $\log(I_{CO(2-1)}/I_{CO(1-0)}) = 0.00\pm0.07$ (corresponding to $I_{CO(2-1)}/I_{CO(1-0)} \sim 1.0$) for the central position and a slightly lower value of $\log(I_{CO(2-1)}/I_{CO(1-0)}) = -0.07 \pm 0.05$ (corresponding to $I_{CO(2-1)}/I_{CO(1-0)} \sim 0.85$) for the off-centre positions. In the calculation of the mean values we did not take into account those objects/positions where both lines are upper limits and we did not attempt to correct for the different beam sizes. We did not find any correlations of this line ratio with other parameters and do not discuss it further in this paper.

4.2. Molecular gas masses

We calculate the molecular gas mass, M_{H_2}, from the CO(1–0) emission using the following equation:

$$M_{H_2} = 75 \times D^2 I_{CO(1-0)} \Omega \quad (2)$$

in $M_\odot$. Here, Ω is the area covered by the observations in arcsec^2 (i.e. $\Omega = 1.13\theta^2$ for a single pointing with a Gaussian beam where θ is the HPBW), D is the distance in Mpc and $I_{CO(1-0)}$ is the velocity integrated line intensity in K km s^{-1}. This equation assumes a CO-to-H_2 conversion factor $X = N_{H_2}/I_{CO} = 2 \times 10^{20}$ cm^{-2} (K km s^{-1})$^{-1}$ (e.g. Dickman et al. 1986). No correction factor for the fraction of helium and other heavy metals is included.

For most of the galaxies only an observation at the centre of the galaxy was obtained so that a correction for emission outside of the beam is necessary in order to derive the total molecular gas mass. We carried out this aperture correction in the same way as described in Lisenfeld et al. (2011), assuming an exponential distribution of the CO emission:

$$I_{CO}(r) = I_0 \propto \exp(r/r_e). \quad (3)$$

We adopt a scale length of $r_e = 0.2 \times r_{25}$, where r_{25} is the major optical isophotal radius at 25 mag arcsec^{-2}, following Lisenfeld et al. (2011), who derived this scale length from different studies (Nishiyama et al. 2001; Regan et al. 2001; Leroy et al. 2008) and from their own CO data. These studies are based on spiral galaxies, however, the analysis of the spatial extent of CO in early-type galaxies in the ALTAS^{3D} survey showed that the relative CO extent, normalized to r_{25}, of early-type and spiral galaxies is the same (Davis et al. 2013). We used this distribution to calculate the expected CO emission from the entire disk, taking the galaxy inclination into account (see Lisenfeld et al. 2011, for more details). This approach assumes that the distribution of the molecular gas in galaxies in HCGs is the same as in isolated galaxies. Unfortunately, so far, no observational data exists that could confirm that this assumption is correct for galaxies in this different environment. Indeed, there is no alternative to applying an aperture correction because the molecular gas mass measured in the central pointing represents a different fraction of the total molecular gas mass for each galaxy, depending on its diameter and inclination. Thus, a study of the central molecular gas mass is only meaningful when we are able to compare it with a magnitude that is measured in the same area, as was done in this paper for the comparison of the cold molecular gas mass to the SFR and the warm molecular gas mass.

Table 6. Cold molecular gas mass.

Galaxy	Ref.	$\log(M_{H_2,0})^a$ [$M_\odot$]	$f_{aper}{}^b$	$\log(M_{H_2,tot})^c$ [$M_\odot$]
HCG 6b	1	9.05*	1.51	9.23*
HCG 6c	1	8.80	1.44	8.96
HCG 15a	2	<8.18	1.89	<8.45
HCG 15d	1	<8.32	1.78	<8.57
HCG 25b	1	9.02	1.60	9.23
HCG 25f	1	<8.36	1.15	<8.42
HCG 31ac	3	8.29	1.46	8.45
HCG 40b	2	8.55	1.69	8.78
HCG 40c	1	9.55	1.91	9.83
HCG 40d	3	9.24	1.46	9.41
HCG 44a	3	8.19	3.68	8.75
HCG 44d	2	7.53	2.98	8.01
HCG 47a	3	9.53	1.52	9.71
HCG 47d	1	8.88	1.26	8.98
HCG 55c	1	9.47	1.29	9.58
HCG 56b	1	<8.55	1.45	<8.71
HCG 56c	1	<8.67	1.51	<8.85
HCG 57a	1	9.47	1.91	9.75
HCG 57d	1	9.12	1.32	9.24
HCG 67b	3	9.44	1.56	9.64
HCG 68a	1	8.06	2.59	8.47
HCG 68b	1	<7.47	3.18	<7.97
HCG 68c	1	8.58	4.83	9.27
HCG 79a	3	<8.39	3.89	<8.98
HCG 79b	2	8.12	2.98	8.60
HCG 82b	1	9.01	1.59	9.21
HCG 82c	3	9.67	1.26	9.77
HCG 91a	1	9.79	3.16	10.29
HCG 95c	1	9.53	1.36	9.67
HCG 96a	1	10.03	2.28	10.38
HCG 100a	3	8.98	1.45	9.14

Notes. (*) Tentative detection. (a) Logarithm of the cold H_2 mass (in solar masses) calculated from the observed central $I_{CO(1-0)}$. (b) Aperture correction factor, defined as $M_{H_2,0}/M_{H_2,tot}$. (c) Logarithm of the cold H_2 mass (in solar masses) extrapolated to the emission from the total disk (see text).

References. (1) This work; (2) Martinez-Badenes et al. (2012); (3) Leon et al. (1998), observed with the IRAM 30 m telescope.

The resulting aperture correction factor, f_{aper}, defined as the ratio between the molecular gas mass observed in the central pointing, $M_{H_2,0}$, and the molecular gas mass extrapolated to the entire disk, $M_{H_2,tot}$, lies between 1.15 and 4.85 with a mean value of 2.0. The values for the molecular gas mass in the central pointing, the extrapolated molecular gas mass and the aperture correction factor are listed in Table 6. In order to test whether biases might be introduced by the aperture correction, we also carried out, as far as possible, all the analysis based on the extrapolated molecular gas masses only for those galaxies where the aperture correction factor was small. In particular, we calculated the mean values for the total molecular gas, $M_{H_2,tot}$, and the ratio M_{H_2}/L_K, listed in Table 7, with the restriction of $f_{aper} < 1.6$ for the subsample of MOHEGs, non-MOHEGs, early type and spiral galaxies. The number of galaxies in the corresponding subsample was

Table 7. Mean values and their errors of $M_{H_2,tot}$ and $M_{H_2,tot}/L_K$ for different subsamples.

Name	T(RC3)[a]	$\log(M_{H_2,tot})$ $[M_\odot]$	n/n_{up}[b]	$\log(M_{H_2,tot}/L_K)$ $[M_\odot/L_{\odot,k}]$	n/n_{up}[b]
MOHEG	all T	8.72 ± 0.18	14/6	–2.16 ± 0.13	13/5
	$T \leq 0$	8.37 ± 0.17	8/5	–2.45 ± 0.11	7/4
	$T \geq 1$	9.24 ± 0.16	6/1	–1.78 ± 0.12	6/1
non-MOHEG	all T	9.32 ± 0.20	13/1	–1.55 ± 0.08	12/1
	$T \leq 0$	8.94 ± 0.18	4/1	–1.86 ± 0.10	4/1
	$T \geq 1$	9.52 ± 0.25	9/0	–1.41 ± 0.06	8/0
all	$T \leq 0$	8.52 ± 0.15	14/7	–2.26 ± 0.12	12/6
	$T \geq 1$	9.36 ± 0.16	17/1	–1.57 ± 0.07	16/1
AMIGA[c]	$T \leq 0$	8.03 ± 0.12	23/15	–2.32 ± 0.10	22/15
	$T \geq 1$	8.38 ± 0.09	150/64	–1.76 ± 0.05	135/50

Notes. [(a)] Morphological subsample. [(b)] Total number of galaxies in the subsample (n) and number of upper limits for the considered magnitude (n_{up}). [(c)] AMIGA sample of isolated galaxies (data from Lisenfeld et al. 2011). The mean values were calculated with ASURV.

about half the total size which made a finer subdivision impossible. The mean values of the restricted subsamples were in very good agreement with those of the total sample.

In Fig. 2 we show the molecular gas mass as a function of morphological type for our sample. Included in the figure are the mean and median values for a sample of ~200 isolated galaxies (Lisenfeld et al. 2011) from the AMIGA (Analysis of the Interstellar Medium of Isolated Galaxies) project (Verdes-Montenegro et al. 2005). The molecular gas masses were obtained in the same way as here, by an extrapolation from observations of CO(1–0) from a central pointing. In Table 7, the mean values[3] of the molecular gas for different subsamples are listed.

The mean molecular gas mass for MOHEGs is lower than the average molecular gas mass for non-MOHEGs. This is partly due to the fact that most MOHEGs are early-type galaxies which have lower average molecular gas masses in all samples considered here. When comparing the mean values of the molecular gas mass for the same group of morphological types, we find for early-type galaxies that MOHEGs have a mean value lower by 0.57 dex (2.3σ) than non-MOHEGs, whereas for spiral galaxies both groups have identical mean values within the errors.

The molecular gas masses of our sample cannot be directly compared to those of the isolated galaxies because of the different mean distances of both samples. Whereas our HCG sample includes objects between 33 and 216 Mpc, the sample of isolated galaxies is restricted to more nearby objects with distances up to 70 Mpc. As a consequence, the galaxies in the HCG are on average brighter in all wavelength, and, indeed, we find that the molecular gas masses of our sample are well above the values found for isolated galaxies.

However, we can compare relative properties. In both samples, early-type galaxies have a lower mean molecular gas mass than spirals. For isolated galaxies, the difference is 0.35 dex (2.3σ), very similar to the difference found in non-MOHEG galaxies in HCGs of 0.58 dex (1.8σ). For MOHEGs in HCGs, the difference is, however, much larger with spiral galaxies having a mean molecular gas mass of 0.87 dex (3.7σ) higher than early-type galaxies.

In summary, we find indications for a lower molecular gas mass in MOHEG early-type galaxies compared to non-MOHEGs early types, and for an unusually large differences (when compared to non-MOHEGs or to isolated galaxies) in molecular gas mass between early-type and spiral MOHEG galaxies. In Sect. 4.7 we continue to investigate this issue by using the distance-independent ratio $M_{H_2,tot}/L_K$.

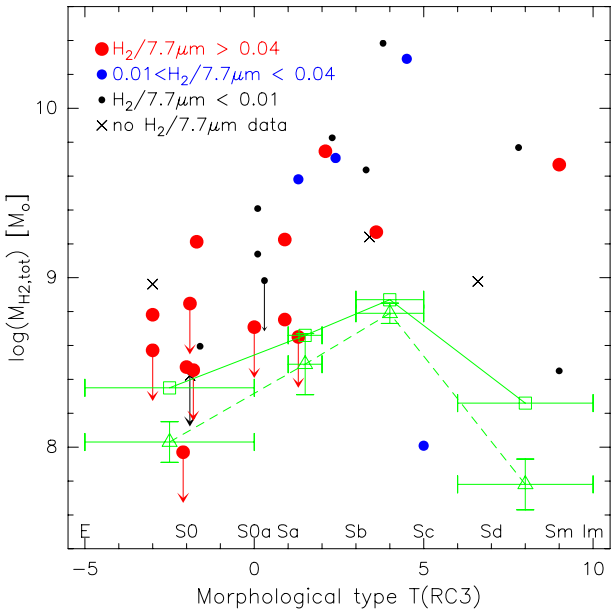

Fig. 2. Total extrapolated molecular gas mass, $M_{H_2,tot}$, as a function of morphological type. Galaxies classified as MOHEGs (H_2/7.7 μm $\geq$ 0.04) are shown as large red circles, non-MOHEG galaxies with 0.01 < H_2/7.7 μm < 0.04 as smaller blue circles, galaxies with H_2/7.7 μm < 0.01 as black dots and galaxies with no warm H_2 data are black crosses. The green symbols denote means (triangles) and medians (squares) for a sample of isolated galaxies (Lisenfeld et al. 2011). The mean, respectively median, are taken for the interval of morphological types shown by the horizontal bar.

4.3. Total mapped molecular gas mass

We determined the total molecular gas mass for the mapped galaxies and compared it to the value obtained from the extrapolation. We calculated the total molecular gas mass by averaging the spectra over the positions where CO was detected. The total molecular gas mass was then calculated from Eq. (2) where Ω is

[3] When calculating the mean values we take upper limits into account by using the program ASURV (Astronomical Survival Analysis) Rev. 1.1 (Lavalley et al. 1992) which is a generalized statistical package that implements the methods presented by Feigelson & Nelson (1985).

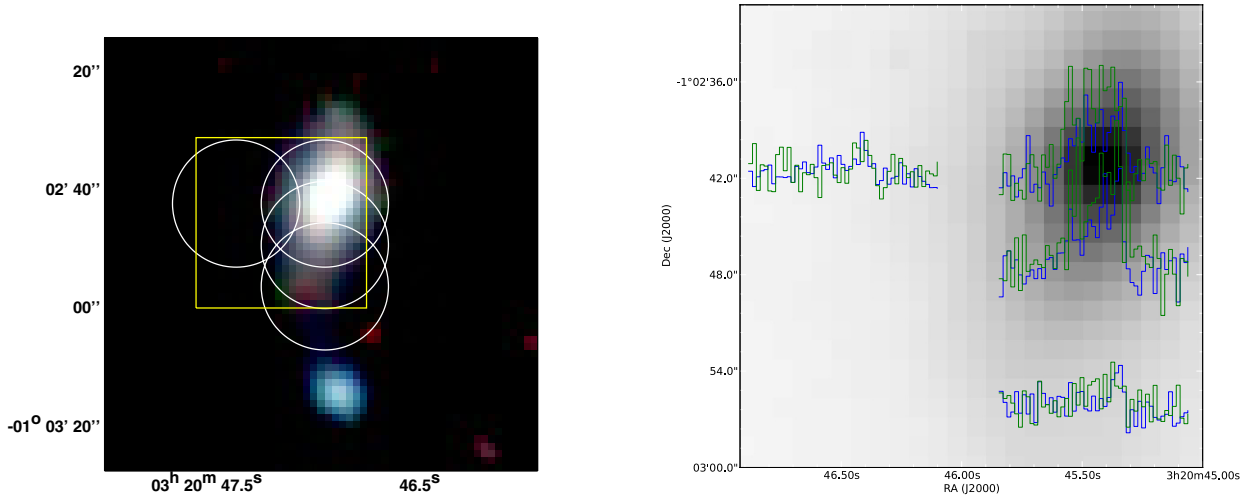

Fig. 3. *Left*: three-color IRAC image (blue is the 3.6 μm, green the 4.5 μm and red the 8 μm band) of HCG 25b. The circles represent the positions detected in CO(1–0). The size of the circles corresponds to the FWHM size of the IRAM 30 m beam at the frequency of CO(1–0). The large yellow rectangle shows, for reference, the size of the zoomed image at the right. *Right*: the detected CO(1–0) (blue) and CO(2–1) (green) spectra at these positions, overlaid over an IRAC 3.5 μm image. The velocity range is from 5600 to 7200 km s^{-1} for all spectra.

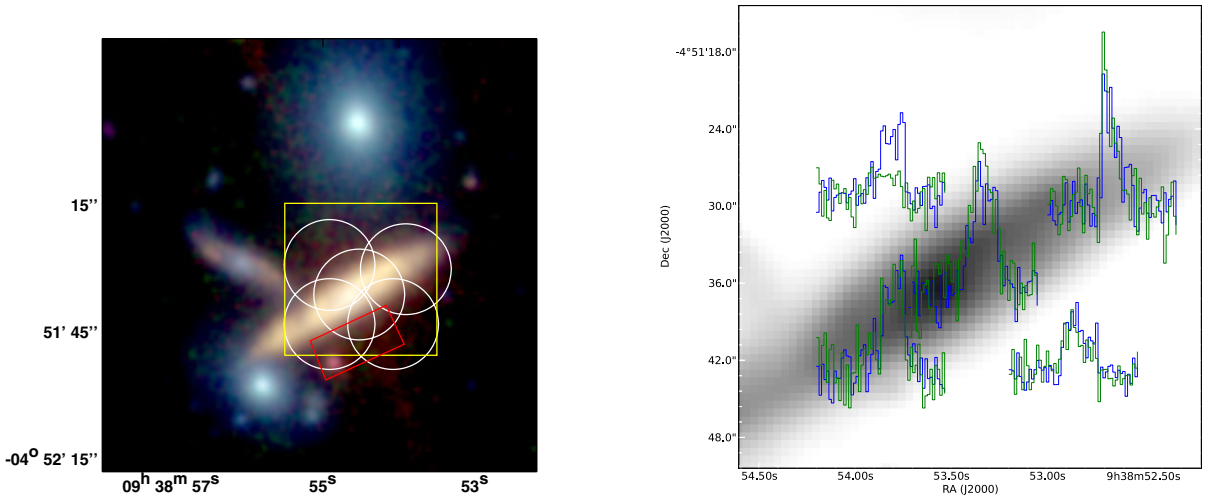

Fig. 4. *Left*: three-color IRAC image (blue is the 3.6 μm, green the 4.5 μm and red the 8 μm band) of HCG 40c. The circles represent the positions detected in CO(1–0). The size of the circles corresponds to the FWHM size of the IRAM 30 m beam at the frequency of CO(1–0). The large yellow rectangle shows, for reference, the size of the zoomed image at the right. The small red rectangle is the position where extragalactic, warm H_2 was detected by Cluver et al. (2013). *Right*: the detected CO(1–0) (blue) and CO(2–1) (green) spectra at these positions, overlaid over an IRAC 3.5 μm image. The velocity range is from 5500 to 7200 km s^{-1} for all spectra.

the total area covered by the beams. In Table 8 we list the total molecular gas mass and compare it to the extrapolated value.

The agreement is reasonable, with a maximum difference of a factor of 1.4 in the case of HCG 25, giving support to the reliability of the aperture correction that was applied to the galaxies.

4.4. Distribution of the molecular gas

In Figs. 3–6 we show the distribution of the spectra within and around the mapped galaxies. In all cases, the CO distribution is extended and, at least slightly, asymmetric.

The CO(1–0) distribution in HCG 25b (Fig. 3) is concentrated mostly in a north-south direction. Emission is also found towards the east (positons (15, 0) and tentatively at (15, –15)) which is the side where the HI shows more emission (Verdes-Montenegro et al., in prep.).

Table 8. Mapped and extrapolated molecular gas mass.

Name	Area[a] [$''^2$]	$M_{H_2,mapped}$[b] [10^9 $M_\odot$]	$M_{H_2,tot}$[c] [10^9 $M_\odot$]	$\frac{M_{H_2,extra}}{M_{H_2,mapped}}$
HCG 25b	1292	1.2	1.7	1.4
HCG 40c	1547	6.4	6.8	1.1
HCG 57a	2547	6.9	5.6	0.8
HCG 91a	3055	16.6	19.5	1.2

Notes. [(a)] Area covered by the beams over which the CO(1–0) intensity was averaged. [(b)] Molecular gas mass determined from the mapping. [(c)] Molecular gas mass determined from the extrapolation of the central value.

The distribution of the CO emission in HCG 91a (Fig. 6) is very asymmetric. There is a pronounced maximum in the north, towards HCG 91c where the spectrum is not only stronger, but

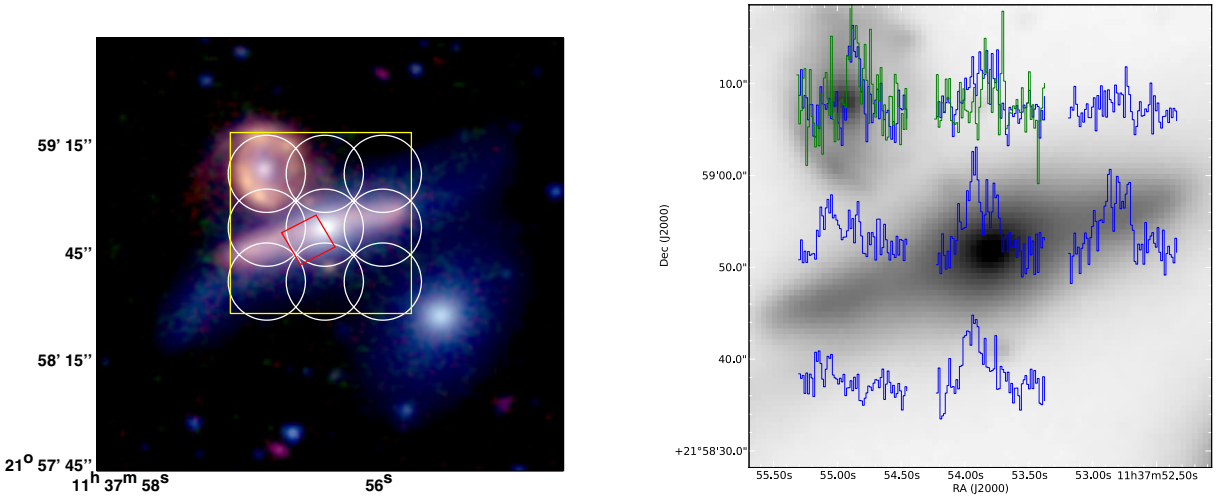

Fig. 5. *Left*: three-color IRAC image (blue is the 3.6 μm, green the 4.5 μm and red the 8 μm band) of HCG 57a (southern object) and 57d (northern object). The circles represent the positions detected in CO(1–0). The size of the circles corresponds to the FWHM size of the IRAM 30 m beam at the frequency of CO(1–0). The large yellow rectangle shows, for reference, the size of the zoomed image at the right. The small red rectangle is the position where extragalactic, warm H_2 was detected by Cluver et al. (2013). *Right*: the detected CO(1–0) (blue) and CO(2–1) (green) spectra at these positions, overlaid over an IRAC 3.5 μm image. The velocity range is from 8000 to 10 000 km s^{-1} for all spectra.

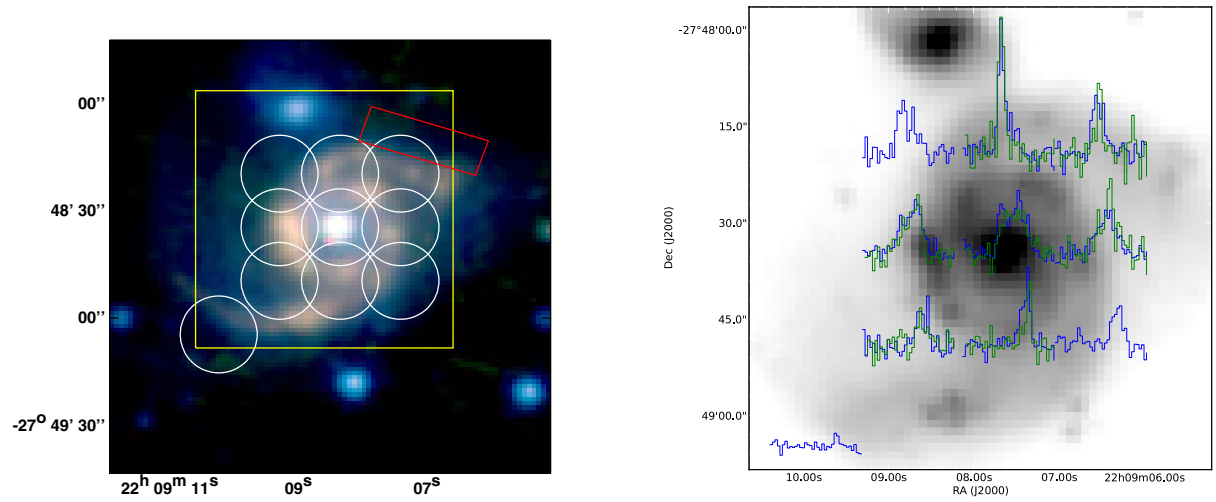

Fig. 6. *Left*: three-color IRAC image (blue is the 3.6 μm, green the 4.5 μm and red the 8 μm band) of HCG 91a. The circles represent the positions detected in CO(1–0). The size of the circles corresponds to the FWHM size of the IRAM 30 m beam at the frequency of CO(1–0). The large yellow rectangle shows, for reference, the size of the zoomed image at the right. The small red rectangle is the position where extragalactic, warm H_2 was detected by Cluver et al. (2013). *Right*: the detected CO(1–0) (blue) and CO(2–1) (green) spectra at these positions, overlaid over an IRAC 3.5 μm image. The velocity range is from 6300 to 7500 km s^{-1} for all spectra.

also very peaked (position 0, 15). There is also considerable emission towards the NW of the galaxy (position –15, 15), close to the place where Cluver et al. (2013) found extragalactic mid-infrared rotational H_2 emission (see red square in Fig. 6).

In HCG 40c (Fig. 4) we find some evidence for extraplanar CO. There is CO(1–0) and CO(2–1) emission detected at two positions about 10.5″ (corresponding to 4.6 kpc at the distance of HCG 40c) above the disk. The CO(1–0) integrated emission is very similar for both positions, of about half the central emission (0.54 ± 0.05 for the NE and 0.49 ± 0.04 for the SW position). Since the FWHM of the CO(1–0) is large compared to the offset, we still expect to detect this level of emission even if the CO is very concentrated towards the disk of the galaxy. The CO(2–1) emission with its smaller beam is more sensitive to variations in spatial scales. Here, we found about twice as much emission in the SW position than in the NE. The emission in the SW is about 0.32 ± 0.04 times the emission of the central position, which is about 3 times the amount that would be expected if the CO distribution is completely concentrated to the galactic plane. The off-plane CO(2–1) emission could be explained with an exponential CO distribution with a scale-height of 5″, corresponding to 2.2 kpc at the distance of HCG 40. This is an unusually large scale height and an indication for off-planar molecular gas. Interestingly, the SW position overlaps with the place where Cluver et al. (2013) found extragalactic warm H_2 emission (see red square in Fig. 4). There might be a relation between both molecular gas emissions, but the poor spatial resolution of our data does not allow us to draw any firm conclusions.

4.5. Ratio between warm and cold molecular gas mass

Figure 7 shows the relation between the warm and cold molecular gas mass in the centres of the galaxies. The cold molecular gas mass corresponds to the mass measured in the central

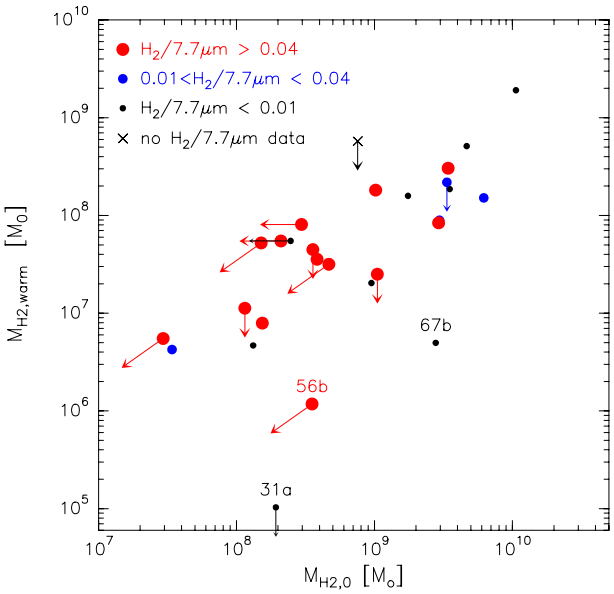

Fig. 7. Warm vs. cold molecular gas masses, both for the central pointing. The green line shows the relation $M_{H_2,warm} = 0.1\ M_{H_2,0}$.

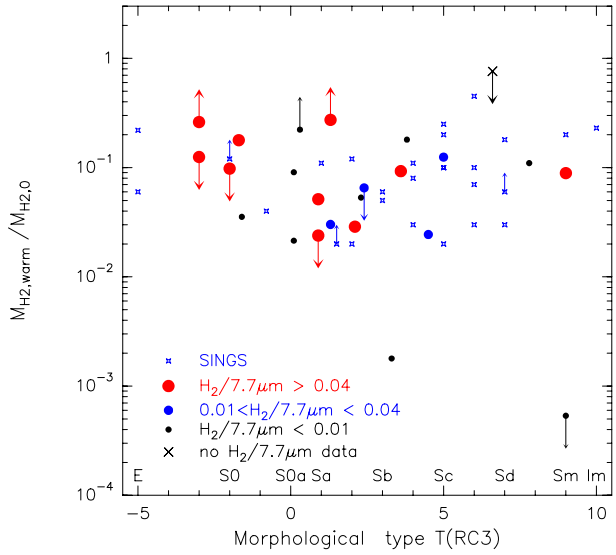

Fig. 8. Warm-to-cold molecular gas mass ratio as a function of morphological type.

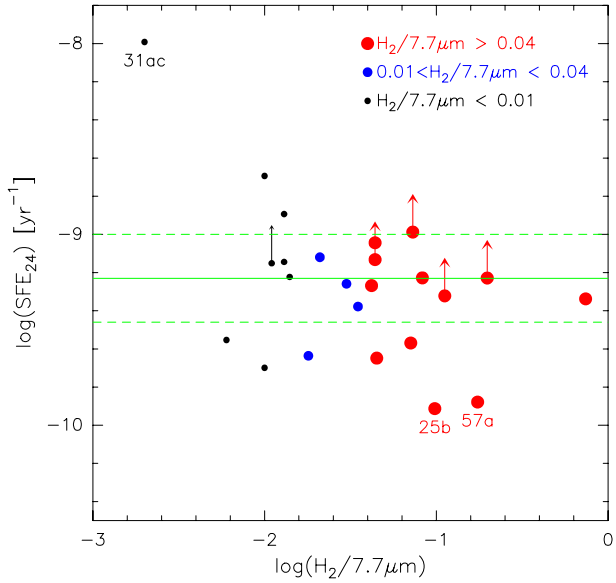

Fig. 9. SFE within the central CO beam as a function of H_2/7.7 μm. The full green line shows the average value derived by Bigiel et al. (2011) for a sample of spiral galaxies and its dispersion (dashed green line).

pointing and the warm molecular gas mass is corrected if the dimension of its emission is larger than the IRAM beam (see Sect. 3.3). There is a correlation between the warm and cold molecular gas mass, albeit with a large scatter, with the warm molecular gas mass being ~1–2 orders of magnitude lower than the cold molecular gas mass. Part of the scatter might be due to uncertainties arising from the correction of the warm molecular gas mass.

We tested the relation between the warm-to-cold molecular gas mass ratio and the morphological type (Fig. 8), and H_2/7.7 μm (not shown here) and no correlation with either of these parameters was found. In this figure we include 31 star-forming galaxies from the SINGS sample whose warm molecular gas properties were studied in Roussel et al. (2007). The range of $M_{H_2,warm}/M_{H_2}$ of the SINGS galaxies coincides very well with the range of our sample.

4.6. SF rates and efficiencies

We chose for our analysis the 24 μm luminosity as the SF tracer, after, as explained in Sect. 3.2, excluding three galaxies where the central 24 μm flux seemed to be affected by an AGN. We calculated the SF rate (SFR) within the IRAM pointing from the 24 μm luminosity, $L_{24\ \mu m,CObeam} = \nu\ f_{24\ \mu m,CObeam} \times 4\pi D^2$, measured within the CO beam as described in Sect. 3.2, adopting the relation derived by Calzetti et al. (2007)

$$SFR_{24\ \mu m}(M_\odot\ yr^{-1}) = 1.27 \times 10^{-38} L^{0.885}_{24\ \mu m,CObeam}(erg\ s^{-1}). \quad (4)$$

This relation assumes a Kroupa (2001) Initial Mass Function (IMF) and was derived from a spatially resolved analysis of the HII regions in 33 galaxies which is adequate for this study which deals with resolved regions of the galaxies. We define the SFE as the ratio between SFR and molecular gas mass, $SFE = SFR_{24\ \mu m}/M_{H_2,0}$, where $M_{H_2,0}$ is the (cold) molecular gas mass within the central pointing.

As a check, we carried out the entire analysis described in this section also for the total SFE, derived from the total 24 μm emission and the extrapolated molecular gas mass. For this case, we calculated the SFR from a relation derived for entire galaxies, $SFR_{24\ \mu m}(M_\odot\ yr^{-1}) = 8.1 \times 10^{-37} L^{0.848}_{24\ \mu m}(erg\ s^{-1})$ (Zhu et al. 2008). We obtained very similar values for the SFE (the mean values agree within 10%) and in general consistent results in comparison to the analysis described in the following. Very similar values (within 10%) and consistent trends were also obtained when calculating the SFR from the 8 μm emission, adopting the relation $SFR_{8\ \mu m}(M_\odot\ yr^{-1}) = 1.2 \times 10^{-43} L_{8\ \mu m}(erg\ s^{-1})$ (Zhu et al. 2008), derived for entire galaxies.

Figure 9 shows the SFE as a function of H_2/7.7 μm. No difference between MOHEGs and non-MOHEG galaxies is found. We neither find variations of the SFE with the IRAC color $f_{5.8}/f_{3.6}$ (not shown) or with the morphological type (Fig. 10). It is interesting that early-type galaxies have the same SFE as spiral galaxies and suggests that they are indeed forming stars in a similar way. This is in contrast to the results of Martig et al. (2013) who found for early-type galaxies from the ATLAS^{3D} that they form stars two to five times less efficiently than a

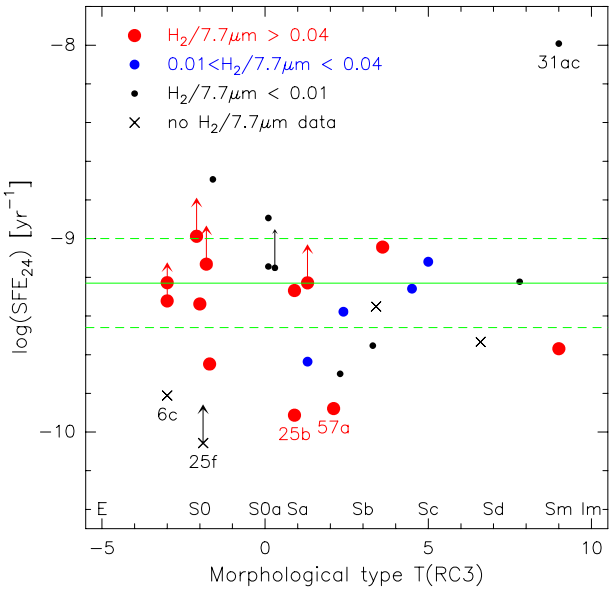

Fig. 10. SFE within the central CO beam as a function of the mophological type. The full green line shows the average value derived by Bigiel et al. (2011) for a sample of spiral galaxies and its dispersion (dashed green line).

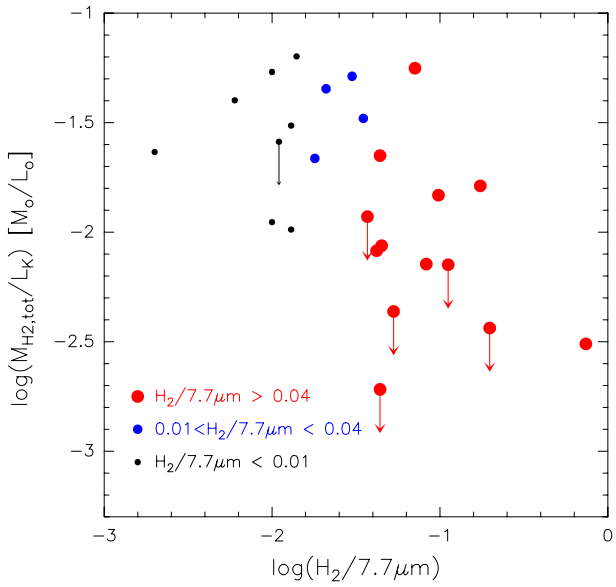

Fig. 11. Ratio between total extrapolated molecular gas mass, $M_{H_2,tot}$, and luminosity in the K band, L_K, as a function of H_2/7.7 μm.

comparison sample of spiral galaxies. The reason for this difference is unclear. We speculate that maybe the different environment of HCGs – gravitational interaction instead of the relatively isolated position of ATLAS^{3D} galaxies – is the reason for this more active SF compared to the molecular gas content.

The mean SFE of our sample is $\log(SFE) = -9.2 \pm 0.1$ yr^{-1} which corresponds to a gas depletion time $\tau_{dep} = (SFE)^{-1}$ of 1.6×10^9 yr. This is very close to the result of Bigiel et al. (2011) who derived $\log(SFE) = -9.23$, with a standard deviation of 0.23, from a spatially resolved analysis of 30 nearby galaxies from the HERACLES survey (the value is adjusted to the Kroupa IMF and no helium fraction). In Figs. 9 and 10 this value and its dispersion are shown as green lines.

The most extreme outliers are HCG 31ac, HCG 25b and HCG 57a. The very high SFE in the merger HCG 31ac (more than an order of magnitude higher than the mean value of Bigiel et al.) is surprising. The SFR derived from the 8 μm emission is 0.4 dex lower than that derived from the 24 μm for this object, so that the discrepancy is less, but still considerable. HCG 31ac is in a very intense phase of SF and classified as a Wolf-Rayet galaxy (O'Halloran et al. 2002). No indication for the presence of an embedded AGN has been found (O'Halloran et al. 2002). Interferometric CO observations with OVRO (Yun et al. 1997) showed that the brightest CO emission is centred in the overlap region between galaxy A and C with a mean surface density of 30 $M_\odot$ pc^{-2}, among the highest of our sample. Given the high-level and spatially concentrated SF present in HCG 31ac, it might indeed be forming stars with a higher SFE.

We also derived the SFEs for the off-centre positions in HCG 25b, HCG 40b, HCG 57a and HCG 91a and were able to look for spatial variations within the galaxies. Whereas in HCG 40b the position at the outskirts of the galaxy have similar values as in the centre, noticeable differences were found in the other galaxies. Lower SFEs were found in the south and western side of HCG 57a, the northern side of HCG 91c, and the eastern position of HCG 25b. In the case of HCG 91a, these positions are on the side where an interacting galaxy and luminous H_2 emission is found (see Fig. 6). In HCG 57a the low SFE and the spatial trend (lower SFE in the centre and west and higher SFE in the east) has been confirmed by CARMA observations (Alatalo et al. 2014). The higher resolution of their data allows the relation of local SF properties to the kinematical properties at those positions. The low SFEs in the centre and western part coincide with peculiar kinematics of the CO with clear deviations from a pure rotation which is most likely due to interaction with HCG 57d. This coincidence suggests that this interaction might also be the reason for suppression of the SF by kinematically disturbing the molecular gas and making gravitational collapse more difficult. Alatalo et al. furthermore discuss a local decrease of the X-factor as an alternative explanation and conclude that it is unlikely to solely explain the low SFEs.

Similarly to the case of HCG 57a, the low SFE at some positions of the other galaxies might be due to a perturbation of the molecular gas that makes gravitational collapse more inefficient and thereby supresses SF. This explanation is suggestive especially in HCG 91a where the low SFE is towards the companion galaxies and at positions with enhanced H_2 emission indicating the presence of shocks. However, we clearly need higher resolution observations in order to draw any firm conclusion.

4.7. Ratio between $M_{H_2,tot}$ and L_K

We examine the relation between the molecular gas mass and the luminosity in the K-band, L_K, which is a reliable tracer for the stellar mass. Lisenfeld et al. (2011) showed that a roughly linear relation exists between the molecular gas mass and L_K for a sample of isolated galaxies so that the ratio between both quantities can be used as an indicator for the normalcy of the molecular gas content. In this section we compare the values of $M_{H_2,tot}/L_K$ between MOHEG, non-MOHEG and isolated galaxies. The mean values for the different ratios are listed in Table 7.

Figure 11 shows $M_{H_2,tot}/L_K$ as a function of H_2/7.7 μm. MOHEG galaxies show considerably lower values of $M_{H_2,tot}/L_K$ than non-MOHEGs. Since we found no difference in the SFE between MOHEGs, non-MOHEGs and field galaxies, this result is consistent with the findings of Cluver et al. (2013, their Fig. 15) that MOHEGs have the lowest specific SFRs ($sSFR = SFR/L_K$).

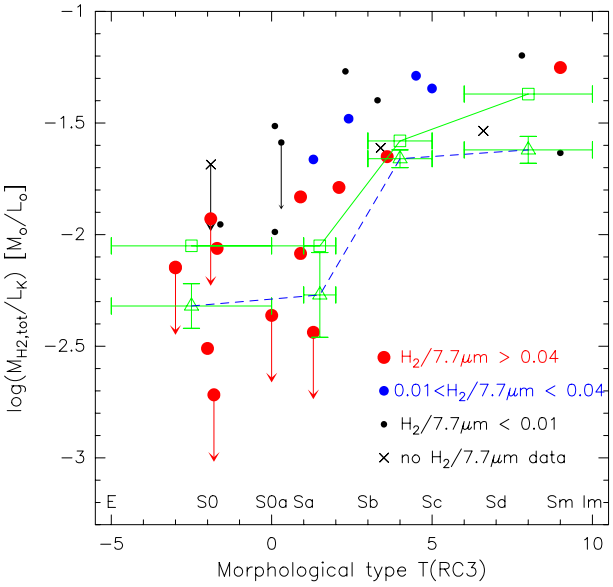

Fig. 12. Ratio between total extrapolated molecular gas mass, $M_{H_2,tot}$, and luminosity in the K band, L_K, as a function of morphological type. The green symbols denote means (triangles) and medians (squares) for a sample of isolated galaxies (Lisenfeld et al. 2011). The mean, respectively median, are taken for the interval of morphological types shown by the horizontal bar.

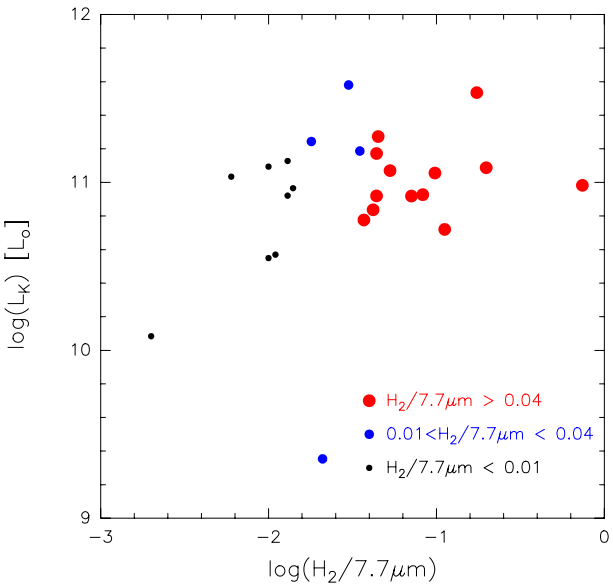

Fig. 13. Luminosity in the K band, L_K, as a function of H_2/7.7 μm.

Figure 12 presents $M_{H_2,tot}/L_K$ as a function of morphological type. The difference in the mean values of $M_{H_2,tot}/L_K$ between MOHEG and non-MOHEG galaxies is at the same time a difference between early-type galaxies (predominatly MOHEGs) and spirals (predominatly non-MOHEGs). We can compare the mean values for early-type galaxies separately for MOHEGs and non-MOHEGs and find (see Table 7) that $M_{H_2,tot}/L_K$ in MOHEG early-type galaxies is 0.59 dex (4σ) lower than in non-MOHEG early-types. When only considering spiral galaxies, MOHEGs also have a lower $M_{H_2,tot}/L_K$ than non-MOHEGs, but the difference is less (0.37 dex, corresponding to 2.8σ). Thus, there are indications, albeit for small subsamples ($n < 10$), that MOHEG galaxies have a lower value of M_{H_2}/L_K compared to non-MOHEG galaxies, independent of their morphological type.

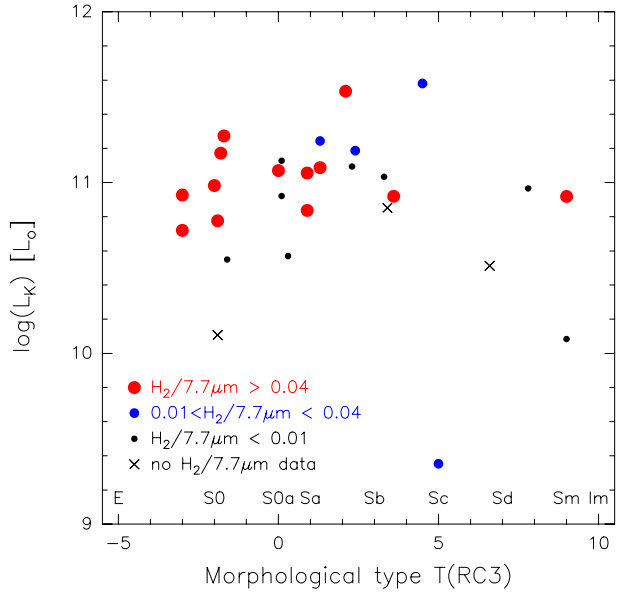

Fig. 14. Luminosity in the K band, L_K, as a function of morphological type.

We include in Fig. 12 the mean and median values for the sample of isolated galaxies from Lisenfeld et al. (2011), mean values are given in Table 7. Spiral galaxies in HCGs have a mean $M_{H_2,tot}/L_K$ which is 0.19 dex (2.2σ) higher than the mean values for isolated spiral galaxies, in agreement with the finding of Badenes-Martinez et al. (2011), who obtained an identical mean value of $M_{H_2,tot}/L_K$ as we for a larger sample of HCG spiral galaxies. The difference is due to the non-MOHEG galaxies, whereas MOHEG spiral galaxies have, within the errors, the same $M_{H_2,tot}/L_K$ as isolated galaxies. Also for early-type galaxies there is good agreement between the values of isolated galaxies and MOHEGs whereas non-MOHEG galaxies tend to have a higher value by 0.46 dex (3.3σ).

The comparatively low $M_{H_2,tot}/L_K$ ratio of MOHEGs is *not* due to a high value in L_K. In Figs. 13 and 14 we show the luminosity in the K-band as a function of H_2/7.7 μm and morphological type, and we find no trend with neither parameter. Thus, MOHEG/early type galaxies have a lower molecular gas mass, which is also evident from Fig. 2 and the results in Sect. 4.1.

An alternative explanation for the lower $M_{H_2,tot}/L_K$ in MOHEGs could be that, instead of having a lower molecular gas mass, their molecular gas is more radially extended than in non-MOHEGs. In this case our extrapolation from the central pointing, outlined in Sect. 4.1, would underestimate the total molecular gas mass. However, although we cannot exclude this possibility, and only the full mapping of the sample will allow us to confirm or discard this option, there is neither observational evidence for a difference in radial extent nor did we find any indications for such a trend when calculating the mean values of Table 7 for the restricted sample of galaxies with $f_{aper} < 1.6$.

4.8. Comparison to group properties

Apart from an analysis of the individual galaxy properties, we furthermore searched for correlations of M_{H_2}/L_K and the SFE with global group properties in order to test whether the group dynamics or its history leaves traces on the molecular gas content or the SF properties of the individual galaxies. Most of the

group parameters that we used for our comparison are listed in Table 1.

We looked for relations with the median projected distance, the crossing time (not listed, from Hickson et al. 1992), the HI mass and the HI deficiency, stellar mass, baryonic mass, the dynamical mass and the compactness traced by different tracers of the group stellar and gas content (blue luminosity, HI mass, stellar mass or the baryonic mass) per area covered by the group. We approximated the baryonic mass as the sum of stellar mass and HI mass, neglecting the contribution of the molecular gas because the latter is generally less than the HI. Furthermore, existing observations of the molecular gas do not cover all members of the group so that only a lower limit to the total molecular gas content can be obtained. In addition, we looked for trends with the evolutionary phase of the groups. We used the classification by Bitsakis et al. (2011) who based it on the relative number of early and spiral galaxies and also the classification by Borthakur et al. (2010) based on the HI distribution in the group. Both classifications are in overall agreement, but whereas the classification of Bitsakis et al. (2011) is available for 16 of our 18 groups, the classification of Borthakur et al. (2010) exists only for 9 groups.

There are some trends of group properties which are due to a relation with the morphological type of galaxies. E.g. in the late evolutionary phase, as defined by Bitsakis et al. (2011) there are more early type galaxies, which are preferably MOHEGs and have a lower value of $M_{\rm H_2}/L_K$. In order to avoid these kind of dependencies we carried out our analysis separately for early type ($T \leq 0$) and spiral ($T \geq 1$) galaxies. For the SFE we found no trends with any of the analyzed group properties, neither for spirals nor for early type galaxies. A similarly negative result was obtained for $M_{\rm H_2}/L_K$ in the subsample of spiral galaxies, but for early type galaxies (which contained $n = 12$ galaxies with 6 upper limits in $M_{\rm H_2,tot}$) we did find some trends. For this subsample, there might be a weak trend of $M_{\rm H_2}/L_K$ to increase with the compactness (as traced by any of the above parameters) of the group which will, however, need to be confirmed with a larger sample. A stronger trend was found for $M_{\rm H_2}/L_K$ to decrease with $M_{\rm dyn}$ and the velocity dispersion of the group. Here, the mean $M_{\rm H_2}/L_K$ for the $n = 6$ galaxies with the lowest values of $M_{\rm dyn}$ or velocity dispersion is 3.9σ above the mean $M_{\rm H_2}/L_K$ for the $n = 6$ galaxies with the highest values. This trend could, however, be due to the fact that practically all galaxies with a low $M_{\rm dyn}$ or a low velocity dispersion are non-MOHEGs whereas practically all galaxies with a high $M_{\rm dyn}$ or velocity dispersion are MOHEGs. It is therefore not clear whether the trend is really between the group property ($M_{\rm dyn}$ or velocity dispersion) and $M_{\rm H_2}/L_K$ or rather between the group property and the presence of enhanced H_2 emission which correlates with $M_{\rm H_2}/L_K$. Thus, we conclude, that although we found some trends for the subsample of early type galaxies studies with larger samples are needed to confirm or reject them.

5. Discussion

5.1. Comparison to other systems

In this paper, we have studied the properties of the cold molecular gas and compared them to those of the warm molecular gas. In order to draw further conclusions about their relation and in particular the excitation mechanism of H_2, it is instructive to compare our results to two well-studied systems where the observational situation allows a good assessment of the processes that are at play.

HCG 92 (Stephan's Quintet, hereafter SQ) contains a kpc-size ridge which exhibits a very high H_2 luminosity caused by a galaxy colliding with intragroup gas. The presence of shocks can be clearly inferred from various indicators as X-ray emission from a hot post-shock plasma (Trinchieri et al. 2003, 2005), radio synchrotron emission (e.g., Sulentic et al. 2001; Williams et al. 2002) from cosmic ray electrons accelerated in the shocks or excitation diagnostics from the optical (Xu et al. 2003) and mid-IR (Cluver et al. 2010) emission. Apart from warm molecular gas, abundant cold (i.e. CO traced) molecular gas is present (Guillard et al. 2012). Guillard et al. (2009) modelled the warm H_2 emission and showed that it is most likely powered by the dissipation of kinetic turbulent energy produced by shocks. In order for this process to work the energy injected on large scales by the collision must cascade on smaller scales which is possible in a multi-phase ISM.

Another system with strong H_2 emission is the bridge between the Taffy galaxies (Condon et al. 1993, 2002), a system of two galaxies which have just experienced a face-on collision. The presence of strong synchrotron emission in the bridge region strongly suggests the presence of shocks accelerating cosmic rays (Lisenfeld & Völk 2010). Peterson et al. (2012) carried out a study of the warm and cold molecular gas in the bridge and concluded that, similar to SQ, the most likely excitation mechanism are shocks powered by kinetic energy injected in the collision.

In both systems the observations clearly show that collisions have taken place and have produced shocks. These processes provide the power for the warm H_2 emission. Is it possible that in our systems similar processes are taking place?

Our sample lacks the spatial resolution in CO and the large amount of ancillary data necessary to directly see whether a gas dynamic interaction and shocks are present. However, we can at least test whether such a scenario would be possible from an energetical point of view. If the dominant energy input is given by shocks and turbulent energy, then these energy sources must be able to balance the cooling rate which is given by the H_2 luminosity. The turbulent heating rate can be written as $\Gamma_{\rm turb} = \frac{3}{2} M_{\rm H_2,warm} \sigma_{\rm T}^3 / l$ (Mac Low 1999) where $\sigma_{\rm T}$ is the H_2 velocity dispersion and l the characteristic length over which the velocity dispersion is measured. Following Guillard et al. (2009), we can then make a rough estimate whether such a process is energetically possible by calculating the turbulent heating rate and requiring

$$\frac{3}{2}\frac{\sigma_{\rm T}^3}{l} \geq \frac{L({\rm H_2})}{M_{\rm H_2,warm}}. \quad (5)$$

We cannot determine $\sigma_{\rm T}$ from the observations because disentangling the turbulent velocity field from the galaxy rotation and tidal effects requires high spatial resolution observations, but we can compare our values of $L({\rm H_2})/M_{\rm H_2,warm}$ (where we compiled $L({\rm H_2})$ from Table 2 in Cluver et al. 2013) to those of SQ and the Taffy bridge. The ratio $L({\rm H_2})/M_{\rm H_2,warm}$ for the galaxies in our sample ranges from 0.03 to 0.3 $L_\odot\, M_\odot^{-1}$. For the ridge in SQ the ratio is $L({\rm H_2})/M_{\rm H_2,warm} = 0.1 \pm 0.02$ $L_\odot\, M_\odot^{-1}$ (Guillard et al. 2012) and for the Taffy bridge $L({\rm H_2})/M_{\rm H_2,warm} = 0.08$ $L_\odot\, M_\odot^{-1}$ (Peterson et al. 2012) , i.e. in both systems the values are in the range of our sample.

In a further crude test to examine the energy that could be available in shocks we compare the kinetic energy in the cold molecular gas $M_{\rm H_2,0}$ to the cooling rate $L({\rm H_2})$ by adopting a corresponding relation as Eq. (5) for the cold molecular gas. The spatial resolution of our data does not allow us

to derive the turbulent velocity dispersion (the line width is mainly driven by rotation) or dissipation scale l directly from the CO spectra and therefore we have to rely on plausibility arguments and a comparison to SQ and the Taffy bridge. The ratios $L(H_2)/M_{H_2,0}$ for our galaxies range between 0.003 and 0.04 $L_\odot\, M_\odot{}^{-1}$ which is somewhat lower than the corresponding values for SQ (0.03 $L_\odot\, M_\odot{}^{-1}$) and the Taffy bridge (0.06 $L_\odot\, M_\odot{}^{-1}$). The higher values for the two latter objects is due to their high warm-to-cold mass ratio ($M_{H_2,warm}/M_{H_2}$= 0.3 for SQ and 0.7 for the Taffy bridge).

In order to quantify our estimate further, we calculate from Eq. (5), assuming that the kinetic energy dissipates in our galaxies over a scales of 1 kpc (a size plausible for a collision with an intragroup gas cloud), the velocity dispersion necessary to power the H_2 luminosity. We derive a range of ~20–55 km s^{-1}, which is much smaller than our CO line widths and thus easily possible to be present.

Therefore, even though spatial resolution of the CO data is not sufficient to firmly decide where the perturbations in the CO and the H_2 emission come from, we can conclude that shocks produced by a collision with intragroup gas are an energetically feasible option.

5.2. The role of CO for the evolution of galaxies in HCGs

The results of Cluver et al. (2013) showed that MOHEG galaxies in HCGs are in a short transition phase between star forming, blue (spiral) galaxies and quiescent, red (early-type) galaxies. This might be a coincidence or it might indicate that the process responsible for the elevated H_2 emission is somehow related to the morphological transition. Cluver et al. (2013) discuss different possible processes that could produce the shocks responsible for the elevated H_2 emission, and conclude that the most likely is an interaction with the intergalactic medium, possibly in the form of viscous stripping. How do our results fit into this picture?

Apart from the energetical argument discussed in the previous subsection, our CO measurements show several pieces of evidence that are consistent with this general scenario. The CO distribution in the mapped objects is in three cases clearly asymmetric (HCG 91a, HCC 57a, HGC 25b) with strong, narrow lines towards a position where warm H_2 was detected (HCG 91a). There is evidence for CO emission with a high scale-height above the disk in HCG 40b, also towards a position with enhanced H_2. The low SFE in some objects and positions could be an indication for the presence of diffuse kinematically perturbed molecular gas, not actively forming stars. As far as the kinematics of the spectra is concerned, we found that several of the MOHEG galaxies had unusually wide lines (up to ~1000 km s^{-1} at 0-level) with indications of several components. Even though the low spatial resolution makes it difficult to draw firm conclusions about what causes all these features, it is clear that the molecular gas shows abnormalities which might be related to the processes causing the enhanced H_2 emission and the intermediate IRAC colours. Indeed, higher resolution (~5″) CARMA observations of HCG 57a have confirmed the peculiarities of the molecular gas distribution and kinematics and have shown that the motion of part of the molecular gas does not follow the general rotation but is rather due to an inflow or outflow (Alatalo et al. 2014).

Not only the molecular gas distribution and its kinematics, but also the total molecular gas mass shows differences between MOHEGs and non-MOHEGs. We found that both the molecular gas mass as well as $M_{H_2,tot}/L_K$ in MOHEGs is low compared to non-MOHEG galaxies (both early-types and spirals). This could indicate a real decrease in the molecular gas mass or – as we only measured the centre and then extrapolated to the total molecular gas mass assuming a radial scale-length – a more radially extended emission of the molecular gas. Models suggest that S0 galaxies in groups are transformed spiral galaxies (e.g. Quilis et al. 2000). The fact that the stellar masses in both morphological groups are the same, is consistent with this picture, because the stellar mass does not change on short time-scales. In this picture, the lower molecular gas mass of MOHEGs compared to non-MOHEGs would indicate that a decrease in the molecular gas mass might be an important step in the transition from spirals to early-type galaxies. The low sSFR found in early-type HCGs galaxies (Cluver et al. 2013; Bitsakis et al. 2011) would therefore be caused by a decrease in neutral gas, then molecular gas, followed by a decrease in the SF activity. Repeated harassment and tidal stripping could transform late-type disks to early-type disks rapidly.

6. Summary and conclusions

We studied the warm and cold molecular gas mass in a sample of 31 galaxies in 18 HCGs. The cold molecular gas mass, M_{H_2}, is traced by the CO(1–0) emission which was mostly observed by us at the IRAM 30 m telescope (for 20 galaxies) and partly taken from the literature (for 11 galaxies). Most galaxies were observed only at their central position, and we extrapolated this measurement to the total molecular gas mass in the disk, $M_{H_2,tot}$, following the prescription of Lisenfeld et al. (2011). Four objects were mapped at several positions over their disks. 27 galaxies have spectroscopic data from the *Spitzer* Space Observatory which allowed us to derive the luminosity and mass, $M_{H_2,warm}$, of the warm molecular gas mass. About half of the sample (14 objects) has a high H_2 luminosity compared to the PAH emission at 7.7 μm, well above the level expected from SF and most likely excited by shocks, and are classified as MOHEGs. Nine galaxies have levels of their H_2 emission expected from SF and the remaining four galaxies have elevated H_2 emission at an intermediate level.

The goal of this study was to characterized the properties of the cold molecular gas in these objects, compare them to those of the warm molecular gas and to look for differences between MOHEG and non-MOHEG galaxies that could shed light on the mechanisms that promote the morphological evolution of galaxies in HCG.

The main results of our analysis are:

- The ratio between the warm and cold molecular gas mass is between a few percent and ~50%, covering the same range as found for SINGS galaxies (Roussel et al. 2007). No trend with neither the morphological type nor the MOHEG parameter, H_2/7.7 μm, has been found.
- Some galaxies, most of them MOHEGs, show very broad spectra (up to 1000 km s^{-1}) with irregular shapes and indications of several components, which cannot be explained by pure rotation. This might be indicative of either a projection effect, adding several components within the same beam, or a perturbation of the molecular gas motions in the galaxies.
- In the galaxies where the CO emission has been mapped, we found evidence for an asymmetric distribution (in HCG 25b, HCG 91c, HCG 57a) and for off-planar emission (in HCG 40c). Both the asymmetry and the off-planar emission are in the direction of a position where off-centre H_2 emission was found.

- The SFE in the central positions lies for most cases in the range found for spiral galaxies (Bigiel et al. 2011). In a few objects and at some off-centre positions, the SFE is considerably lower which might indicate the presence of diffuse or kinematically perturbed gas not participating in SF. We found no trend of the SFE with morphological type, H_2/7.7 μm or any tested group parameters (HI mass and deficiency, velocity dispersion, dynamical and stellar masses or compactness). Early-type galaxies in HCGs seems to be forming stars with the same efficiency as spiral galaxies.
- We found evidence for a lower cold molecular gas mass in MOHEG galaxies, compared to non-MOHEG galaxies. Both the molecular gas mass, $M_{H_2,tot}$, as well as the ratio $M_{H_2,tot}/L_K$ was lower than the corresponding value in non-MOHEG galaxies (both for the entire sample and separately for early-types and for spirals). We found a trend for galaxies in groups with a low dynamical mass or velocity dispersion to have a higher $M_{H_2,tot}/L_K$ and to be more likely a non-MOHEG.

These results indicate pecularities in the kinematics, distribution and total content of the cold molecular gas in MOHEGs, compared to non-MOHEG galaxies. The decrease in the molecular gas content is expected to cause a decrease in the SFR, which could produce an evolution of galaxies from blue to the red sequence. Thus, our CO data are consistent with a picture of morphological evolution of galaxies in HCGs in which MOHEGs play a central role as galaxies being in the process of evolution. Furthermore, our data hint to a possible link of these signs of evolution to kinematical perturbations of the molecular gas which appears energized by the dissipation of turbulent energy. However, much higher spatial resolution is needed to prove this picture by locating those perturbations and separating the contributions from tidal effects, in/outflows, and turbulence.

Acknowledgements. This work has been supported by the research projects AYA2011-24728 from the Spanish Ministerio de Ciencia y Educación and the Junta de Andalucía (Spain) grants FQM108. It is based on observations with the Instituto de Radioastronomía Milimétrica IRAM 30 m. This research has made use of the NASA/IPAC Extragalactic Database (NED) which is operated by the Jet Propulsion Laboratory, California Institute of Technology, under contract with the National Aeronautics and Space Administration. We also acknowledge the use of the HyperLeda database (http://leda.univ-lyon1.fr).

References

Abadi, M. G., Moore, B., & Bower, R. G. 1999, MNRAS, 308, 947
Alatalo, K., Appleton, P. N., Lisenfeld, U., et al. 2014, ApJ, submitted
Appleton, P. N., Xu, K. C., Reach, W., et al. 2006, ApJ, 639, L51
Bekki, K. 1998, ApJ, 502, L133
Bekki, K., & Couch, W. J. 2011, MNRAS, 415, 1783
Bekki, K., Couch, W. J., & Shioya, Y. 2002, ApJ, 577, 651
Bigiel, F., Leroy, A. K., Walter, F., et al. 2011, ApJ, 730, L13
Bitsakis, T., Charmandaris, V., da Cunha, E., et al. 2011, A&A, 533, A142
Bitsakis, T., Charmandaris, V., Appleton, P. N., et al. 2014, A&A, 565, A25
Borthakur, S., Yun, M. S., & Verdes-Montenegro, L. 2010, ApJ, 710, 385
Calzetti, D., Kennicutt, R. C., Engelbracht, C. W., et al. 2007, ApJ, 666, 870
Cluver, M. E., Appleton, P. N., Boulanger, F., et al. 2010, ApJ, 710, 248
Cluver, M. E., Appleton, P. N., Ogle, P., et al. 2013, ApJ, 765, 93
Condon, J. J., Helou, G., Sanders, D. B., & Soifer, B. T. 1993, AJ, 105, 1730
Condon, J. J., Helou, G., & Jarrett, T. H. 2002, AJ, 123, 1881
Davis, T. A., Alatalo, K., Bureau, M., et al. 2013, MNRAS, 429, 534
de Vaucouleurs, G., de Vaucouleurs, A., Corwin, Jr., H. G., et al. 1991, 3rd Reference Catalogue of Bright Galaxies (New York: Springer-Verlag)
Dickman, R. L., Snell, R. L., & Schloerb, F. P. 1986, ApJ, 309, 326
Engelbracht, C. W., Blaylock, M., Su, K. Y. L., et al. 2007, PASP, 119, 994
Farouki, R., & Shapiro, S. L. 1980, ApJ, 241, 928
Feigelson, E. D., & Nelson, P. I. 1985, ApJ, 293, 192
Guillard, P., Boulanger, F., Pineau Des Forêts, G., & Appleton, P. N. 2009, A&A, 502, 515
Guillard, P., Ogle, P. M., Emonts, B. H. C., et al. 2012, ApJ, 747, 95
Gunn, J. E., & Gott, III, J. R. 1972, ApJ, 176, 1
Hickson, P. 1982, ApJ, 255, 382
Hickson, P., Mendes de Oliveira, C., Huchra, J. P., & Palumbo, G. G. 1992, ApJ, 399, 353
Icke, V. 1985, A&A, 144, 115
Jarrett, T. H., Chester, T., Cutri, R., et al. 2000, AJ, 119, 2498
Johnson, K. E., Hibbard, J. E., Gallagher, S. C., et al. 2007, AJ, 134, 1522
Kroupa, P. 2001, MNRAS, 322, 231
Larson, R. B., Tinsley, B. M., & Caldwell, C. N. 1980, ApJ, 237, 692
Lavalley, M. P., Isobe, T., & Feigelson, E. D. 1992, in BAAS, 24, 839
Leon, S., Combes, F., & Menon, T. K. 1998, A&A, 330, 37
Leroy, A. K., Walter, F., Brinks, E., et al. 2008, AJ, 136, 2782
Lisenfeld, U., & Völk, H. J. 2010, A&A, 524, A27
Lisenfeld, U., Espada, D., Verdes-Montenegro, L., et al. 2011, A&A, 534, A102
Mac Low, M.-M. 1999, ApJ, 524, 169
Martig, M., Crocker, A. F., Bournaud, F., et al. 2013, MNRAS, 432, 1914
Martinez-Badenes, V., Lisenfeld, U., Espada, D., et al. 2012, A&A, 540, A96
Nishiyama, K., Nakai, N., & Kuno, N. 2001, PASJ, 53, 757
Ogle, P., Boulanger, F., Guillard, P., et al. 2010, ApJ, 724, 1193
O'Halloran, B., Metcalfe, L., McBreen, B., et al. 2002, ApJ, 575, 747
Peterson, B. W., Appleton, P. N., Helou, G., et al. 2012, ApJ, 751, 11
Quilis, V., Moore, B., & Bower, R. 2000, Science, 288, 1617
Regan, M. W., Thornley, M. D., Helfer, T. T., et al. 2001, ApJ, 561, 218
Rigopoulou, D., Kunze, D., Lutz, D., Genzel, R., & Moorwood, A. F. M. 2002, A&A, 389, 374
Roussel, H., Helou, G., Hollenbach, D. J., et al. 2007, ApJ, 669, 959
Sulentic, J. W., Rosado, M., Dultzin-Hacyan, D., et al. 2001, AJ, 122, 2993
Trinchieri, G., Sulentic, J., Breitschwerdt, D., & Pietsch, W. 2003, A&A, 401, 173
Trinchieri, G., Sulentic, J., Pietsch, W., & Breitschwerdt, D. 2005, A&A, 444, 697
Verdes-Montenegro, L., Yun, M. S., Perea, J., del Olmo, A., & Ho, P. T. P. 1998, ApJ, 497, 89
Verdes-Montenegro, L., Yun, M. S., Williams, B. A., et al. 2001, A&A, 377, 812
Verdes-Montenegro, L., Sulentic, J., Lisenfeld, U., et al. 2005, A&A, 436, 443
Verdes-Montenegro, L., Yun, M. S., Borthakur, S., et al. 2007, in Groups of Galaxies in the Nearby Universe, eds. I. Saviane, V. D. Ivanov, & J. Borissova (Springer Verlag), 349
Walker, L. M., Johnson, K. E., Gallagher, S. C., et al. 2010, AJ, 140, 1254
Walker, L. M., Johnson, K. E., Gallagher, S. C., et al. 2012, AJ, 143, 69
Wilgenbus, D., Cabrit, S., Pineau des Forêts, G., & Flower, D. R. 2000, A&A, 356, 1010
Williams, B. A., Yun, M. S., & Verdes-Montenegro, L. 2002, AJ, 123, 2417
Xu, C. K., Lu, N., Condon, J. J., Dopita, M., & Tuffs, R. J. 2003, ApJ, 595, 665
Yun, M. S., Verdes-Montenegro, L., del Olmo, A., & Perea, J. 1997, ApJ, 475, L21
Zhu, Y.-N., Wu, H., Cao, C., & Li, H.-N. 2008, ApJ, 686, 155

Pages 17 to 20 are available in the electronic edition of the journal at http://www.aanda.org

Table 5. Integrated CO intensities.

Galaxy	RA offset [″]	Dec offset [″]	rms[a] [mK]	$I_{CO(1-0)}$ [K km s^{-1}]	$\Delta V_{CO(1-0)}$[b] [km s^{-1}]	rms[a] [mK]	$I_{CO(2-1)}$[c] [K km s^{-1}]	$\Delta V_{CO(2-1)}$[b] [km s^{-1}]
HCG 6b	0	0	2.98	1.13 ± 0.30*	620	3.98	1.78 ± 0.40*	620
HCG 6b	0	15	2.99	<2.37	–	4.77	<3.66	–
HCG 6b	0	–15	3.12	0.58 ± 0.16*	160	3.96	<1.81	–
HCG 6b	15	0	3.04	<2.41	–	4.25	<3.26	–
HCG 6b	–15	0	2.99	<2.37	–	4.87	<3.74	–
HCG 6c	0	0	2.48	0.64 ± 0.15	220	3.64	<1.96	–
HCG 15d	0	0	2.25	<1.77	–	3.82	<2.91	–
HCG 15d	0	15	3.46	<2.73	–	4.94	<3.77	–
HCG 25b	0	0	2.85	3.37 ± 0.26	520	3.80	5.01 ± 0.35	540
HCG 25b	0	–7	2.52	3.56 ± 0.25	600	4.48	5.28 ± 0.42	560
HCG 25b	0	15	3.33	<2.62	–	4.52	<3.45	–
HCG 25b	0	–15	2.03	0.51 ± 0.10	160	2.34	1.08 ± 0.21	520
HCG 25b	0	–23	2.42	<1.91	–	4.14	<3.16	–
HCG 25b	15	0	1.48	1.15 ± 0.14	600	2.44	0.53 ± 0.15*	240
HCG 25b	15	–15	2.62	0.70 ± 0.19*	330	3.43	<2.23	–
HCG 25b[(1)]	–3	–33	2.80	<2.21	–	3.87	<2.96	–
HCG 25b	–15	0	2.53	<2.00	–	3.81	<2.90	–
HCG 25b	–15	–15	4.18	<3.30	–	9.62	<7.34	–
HCG 40c	–3	1	5.69	10.20 ± 0.59	680	8.64	11.83 ± 0.81	540
HCG 40c	4	8	4.28	6.25 ± 0.39	520	5.42	2.33 ± 0.47	460
HCG 40c	4	–6	5.83	8.24 ± 0.53	520	7.81	8.48 ± 0.73	550
HCG 40c	4	–21	4.04	0.54 ± 0.15*	90	5.89	<2.01	–
HCG 40c	34	–36	4.48	1.18 ± 0.35*	380	6.68	<4.69	–
HCG 40c	–11	–6	3.20	5.18 ± 0.28	490	4.80	4.01 ± 0.42	480
HCG 40c	–14	7	5.75	7.14 ± 0.50	480	7.55	6.36 ± 0.52	290
HCG 40c	–18	–14	2.79	<2.20	–	3.68	<2.81	–
HCG 47d	0	0	2.07	1.09 ± 0.13	260	–	–	–
HCG 55c	0	0	1.23	1.54 ± 0.13	730	3.33	2.36 ± 0.34	640
HCG 56b	0	0	2.69	<2.12	–	4.33	<3.31	–
HCG 56c	0	0	3.57	<2.81	–	6.36	<4.85	–
HCG 57a	0	0	2.41	4.57 ± 0.28	840	–	–	–
HCG 57a	0	15	2.00	2.70 ± 0.22	720	3.58	1.63 ± 0.32	490
HCG 57a	0	–15	1.96	3.19 ± 0.21	740	3.26	<3.19	–
HCG 57a	15	0	1.91	2.68 ± 0.22	810	–	–	–
HCG 57a[(2)]	15	15	2.61	2.06 ± 0.19	340	4.85	2.70 ± 0.39	400
HCG 57a	15	–15	1.56	0.99 ± 0.13	440	2.89	1.01 ± 0.23	380
HCG 57a	–15	0	2.30	3.90 ± 0.26	820	–	–	–
HCG 57a	–15	15	2.03	0.60 ± 0.15	360	3.97	<2.71	–
HCG 68a	0	0	1.92	2.59 ± 0.23	960	2.90	5.10 ± 0.35	920
HCG 68b	0	0	2.57	<2.01	–	5.73	<4.34	–
HCG 68c	0	0	4.97	8.67 ± 0.36	340	8.38	12.65 ± 0.65	380
HCG 82b	0	0	1.83	1.13 ± 0.17	500	3.59	<2.91	–
HCG 91a	0	0	6.39	15.81 ± 0.58	520	8.36	14.13 ± 0.83	620
HCG 91a	0	15	9.07	14.20 ± 0.75	430	13.32	10.69 ± 0.71	180
HCG 91a	0	–15	6.81	7.62 ± 0.44	270	10.21	5.28 ± 0.58	200
HCG 91a	15	0	7.50	12.85 ± 0.72	580	8.99	11.25 ± 0.79	490
HCG 91a	15	15	9.51	9.21 ± 0.74	380	27.79	<19.48	–
HCG 91a	15	–15	8.79	5.55 ± 0.59	290	10.88	4.17 ± 0.73	280
HCG 91a	–15	0	8.13	9.66 ± 0.71	470	14.05	11.96 ± 1.19	450
HCG 91a	–15	15	8.43	9.10 ± 0.67	390	16.29	6.18 ± 1.11	290
HCG 91a	–15	–15	7.55	5.99 ± 0.54	320	21.73	<13.98	–
HCG 91a	30	–30	3.80	0.79 ± 0.17	130	6.73	<2.76	–
HCG 95c	0	0	3.04	3.15 ± 0.25	420	5.81	8.75 ± 0.52	490
HCG 95c	0	15	3.44	2.37 ± 0.34	600	4.89	<4.34	–
HCG 96a	0	0	3.38	18.02 ± 0.25	340	4.93	24.24 ± 0.36	320

Notes. [(*)] Tentative detections. [(1)] Coincides with the position of HCG 25f. [(2)] Coincides (within 1″) with the position of HCG 57d. [(a)] Root-mean-square noise at a velocity resolution of 16 km s^{-1}. [(b)] Zero-level line width. The uncertainty is roughly given by the velocity resolution (16 km s^{-1}). [(c)] At some positions the bandwidth did not entirely cover the expected line range so that no value for $I_{CO(2-1)}$ can be given.

Appendix A: Spectra of detected positions

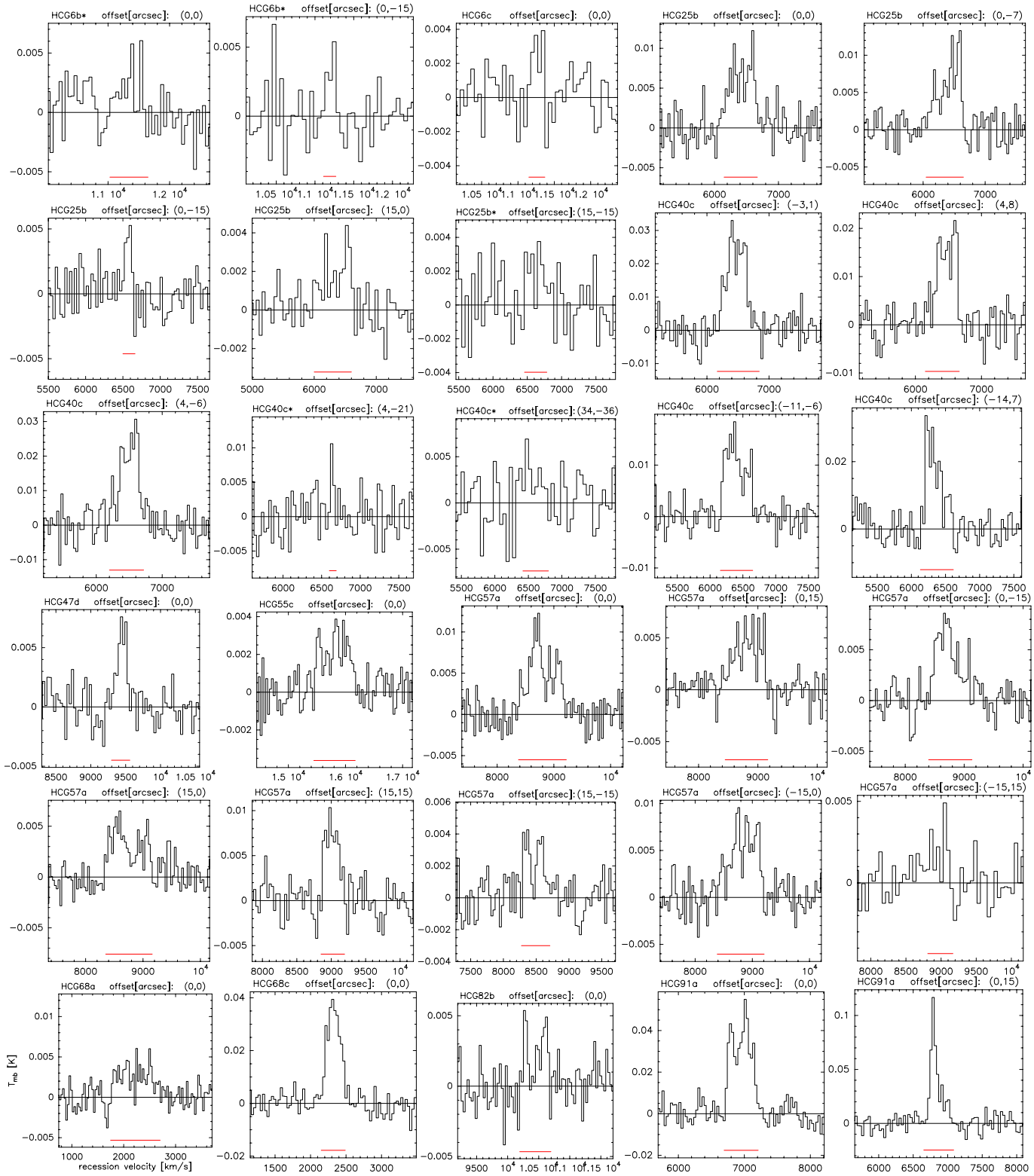

Fig. A.1. CO(1–0) spectra of the detected (including tentative detections) spectra. The velocity resolution is ∼32 km s^{-1} for most spectra and ∼48 km s^{-1} for some cases where a lower resolution was required to clearly see the line. The red line segment shows the zero-level line width of the CO line adopted for the determination of the velocity integrated intensity. An asterisk next to the name indicates a tentative detection.

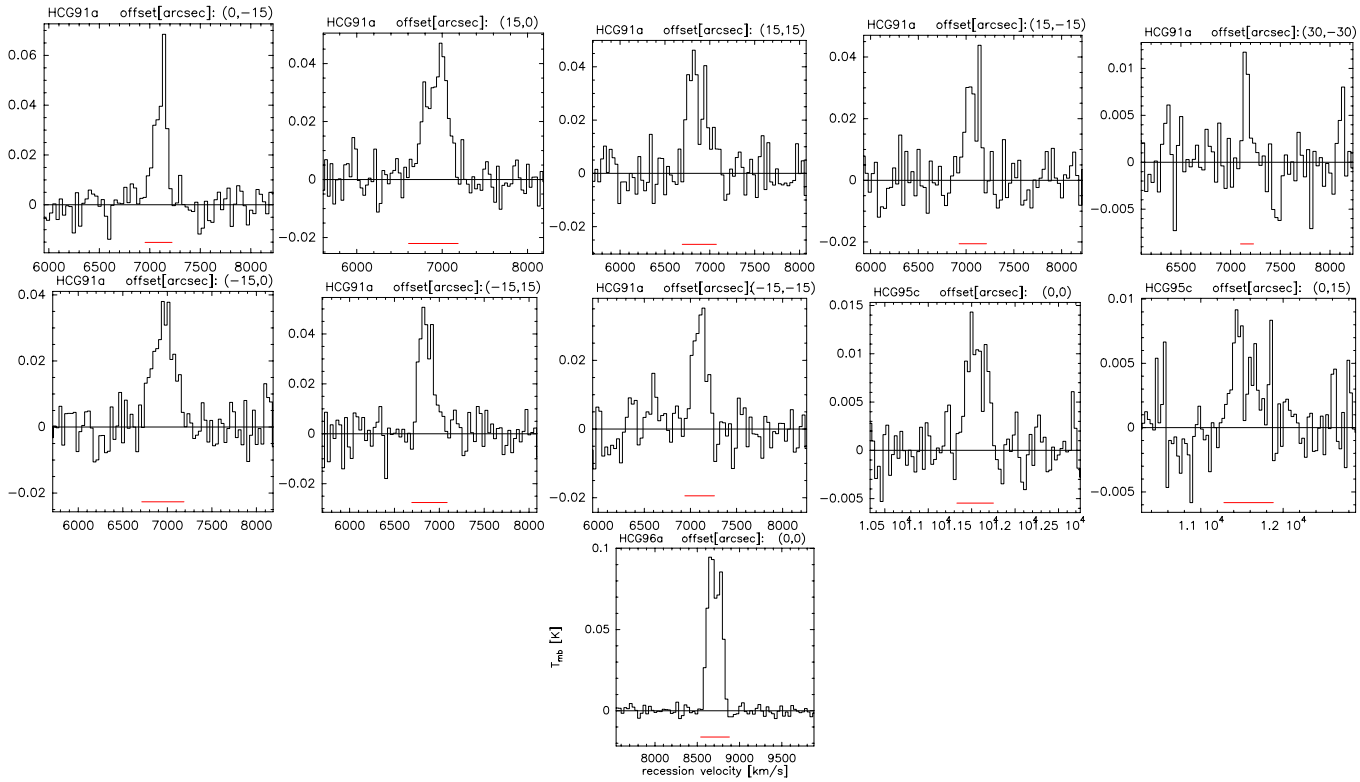

Fig. A.1. continued.

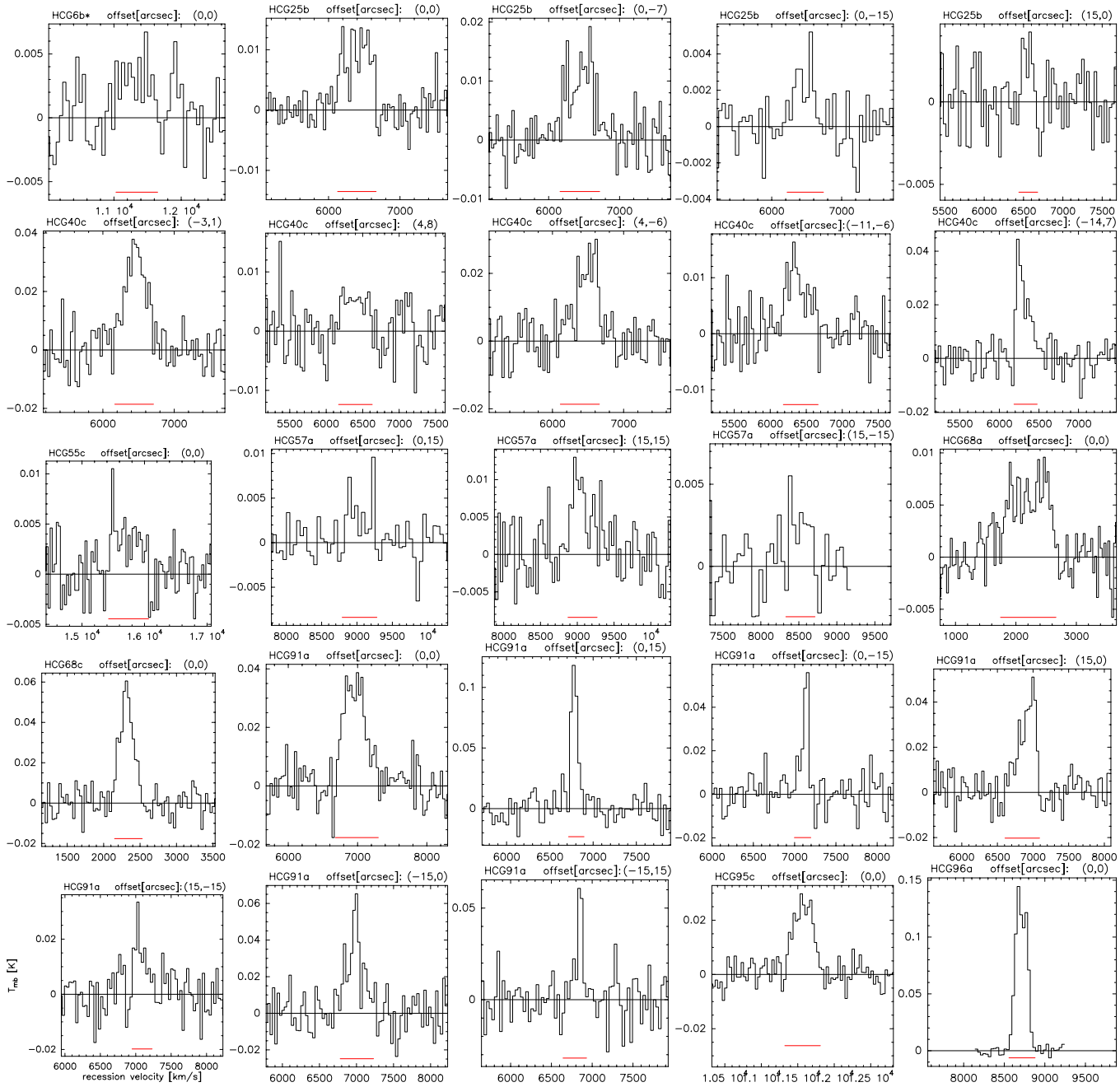

Fig. A.2. CO(2–1) spectra of the detected (including tentative detections) spectra. The velocity resolution is ∼32 km s^{-1} for most spectra and ∼48 km s^{-1} for some cases where a lower resolution was required to clearly see the line. The red line segment shows the zero-level line width of the CO line adopted for the determination of the velocity integrated intensity. An asterisk next to the name indicates a tentative detection.